

A consistent volume-of-fluid approach for direct numerical simulation of the aerodynamic breakup of a vaporizing drop

Bradley Boyd ^{a,b,*}, Yue Ling ^{a,c}

^a Department of Mechanical Engineering, Baylor University, Waco, TX 76798, USA

^b Department of Mechanical Engineering, University of Canterbury, Private Bag 4800, Christchurch 8140, New Zealand

^c Department of Mechanical Engineering, University of South Carolina, 300 Main St, Columbia, SC 29208, USA



ARTICLE INFO

Keywords:

Volume-of-fluid method

Vaporization

Drop breakup

DNS

ABSTRACT

A novel simulation framework has been developed in this study for the direct numerical simulation of the aerodynamic breakup of a vaporizing drop. The interfacial multiphase flow with phase change is resolved using a consistent geometric volume-of-fluid method. The bulk fluids are viscous and incompressible with surface tension at the interface. The newly-developed numerical methods have been implemented in the *Basilisk* solver, in which the adaptive octree/quadtrees mesh is used for spatial discretization, allowing flexibility in dynamically refining the mesh in a user-defined region. The simulation framework is extensively validated by a series of benchmark cases, including the 1D Stefan and sucking problems, the growth of a 3D spherical bubble in a superheated liquid, and a 2D film boiling problem. The simulation results agree very well with the exact solution and previous numerical studies. 2D axisymmetric simulations were performed to resolve the vaporization of a moving drop with a low Weber number in a high-temperature free stream. The computed rate of volume loss agrees well with the empirical model of drop evaporation. Finally, the validated solver is used to simulate the aerodynamic breakup of an acetone drop at a high Weber number. A fully 3D simulation is performed and the morphological evolution of the drop is accurately resolved. The rate of vaporization is found to be significantly enhanced due to the drop deformation and breakup. The drop volume decreases nonlinearly in time and at a much higher rate than the empirical correlation for a spherical drop.

1. Introduction

Direct numerical simulations are crucial to the investigation of a vast array of multiphase flows, such as fuel injection [1] and cavitation [2–4], as they are able to provide high-level details that are difficult to measure in experiments [5]. Accurately resolving the sharp interface separating the gas and liquid phases is critical to interfacial multiphase flow simulations. The methods for numerically resolving the interface are loosely categorized into diffuse-interface and sharp-interface methods. The diffuse-interface methods involve the advection of a volume or mass fraction, which is allowed to diffuse over a few cells, and such methods are more popular for compressible flows [6–9]. For incompressible flows, it is possible to achieve a genuine sharp interface and to constrain the interface thickness to one cell. Significant progress has been made in the development of interface-capturing methods, including the volume-of-fluid (VOF), front-tracking, and level-set methods, in the past decades [10–12]. Now it is viable to accurately simulate multiphase flows with complex interface deformation and topology change, assuming the mesh resolution is sufficiently high.

Multiphase flows with phase change are essential to a wide range of industrial applications, such as the injection of volatile liquid fuels [13] and boiling flows [14]. The inclusion of phase change introduces additional complexities in resolving interfacial multiphase flows. While a transition from liquid to vapor can happen at temperatures below the saturation temperature, (T_{sat}), more rapid vaporization will occur if the phase change happens at the boiling point, T_{sat} . In the present study, we only consider phase change due to vaporization as opposed to condensation [15,16]. More important, we will focus on vaporization that is driven by heat transfer, instead of the slower process of evaporation due to vapor concentration gradients [17,18]. Nevertheless, with minor modifications, the present methods can be used to simulate multiphase flows with condensation and concentration-gradient-driven evaporation.

High-resolution detailed numerical simulations have been shown to be an essential tool to investigate liquid–gas multiphase flows with phase change, and various computational methods have been developed to track the sharp interface with interfacial vaporization. Recent

* Corresponding author at: Department of Mechanical Engineering, University of Canterbury, Private Bag 4800, Christchurch 8140, New Zealand.
E-mail addresses: bradley.boyd@canterbury.ac.nz (B. Boyd), stanley_ling@sc.edu (Y. Ling).

numerical approaches in the literature include front tracking [19], Lattice Boltzmann [20,21], level-set/ghost fluid [18,22,23], and Volume-of-Fluid (VOF) methods [24–36]. We refer the readers to Refs. [37,38] for a more comprehensive review of the numerical approaches to account for phase change.

In the present study, we focus on developing a numerical framework to simulate interfacial multiphase flows with phase change based on the VOF method. The VOF method is based on the one-fluid approach, for which only one velocity field is used for both phases. Without phase change, the velocities for the liquid and gas on the two sides of an interface are identical, and thus the velocities in the cells in the vicinity of the interface are ready to be used to advect the interface. However, when phase change like vaporization occurs, the velocity is discontinuous across the interface, as vaporization creates the Stefan flow in the gas phase. The interface velocity is more similar to the liquid velocity instead of the gas velocity. In such a case, the “one-fluid” velocity field cannot be directly used to advect the volume-fraction function. In the recent works of Malan et al. [36] and Bureš et al. [35], an additional pressure projection step has been used to compute a separate velocity field, *i.e.*, the divergence-free liquid velocity across the interface, which is then used for the VOF advection. It is computationally costly to solve the additional pressure Poisson equation for this additional velocity in the whole domain. As a result, they have included two immersed boundaries on the gas and liquid sides of the interface and only solve the Poisson equation in a reduced region near the interface. Nevertheless, this inclusion of additional immersed boundaries is also undesirable, especially for parallel codes that use a more complicated mesh such as an adaptive octree mesh.

To accurately compute the vaporization rate it is important to solve the thermal diffusion and the temperature field near the interface. The recent works by Gao et al. [39] and Zhao et al. [40] have used the embedded boundary method [41,42] for the thermal flux calculation in each phase. The embedded boundary method typically requires the embedded boundary/surface to be continuous at the cell surfaces. However, this is not guaranteed in the Piece-wise Linear Interface Calculation (PLIC) VOF reconstruction. The different intersecting positions between the cell surface and the reconstructed interfaces from the two adjacent cells create additional complexity in calculating the thermal diffusion flux. Additionally, the temperature gradient near the interface is highly dependent on the normal, which may exhibit small cell-to-cell fluctuations due to the PLIC VOF reconstruction. These two factors are likely the cause of the artificial velocity currents present in [39]. In the method of Zhao et al. [40], the VOF advection is handled using a two-velocity approach, similar to Malan et al. [36], whereas, in the method of Gao et al. [39], they distributed the vaporization-induced source term to nearby pure gas and liquid cells but not the interfacial cells, following the method by Hardt and Wondra [25]. As a result, the velocity at the interfacial cells is not influenced and can be used for the VOF advection. Gao et al. [39] diffused the source to wide regions in both gas and liquid sides of the interface for numerical stability. Yet, velocity fluctuations were still observed near the interfaces.

The goal of the present paper is to develop a simple and robust VOF method to resolve interfacial multiphase flows with vaporization. The long-term goal is to use the newly developed method to fully characterize the breakup dynamics of vaporizing bulk liquids, such as aerobreakup of drops in a high-temperature and high-speed flow through high-fidelity simulation. Extensive experimental and numerical studies have been conducted to understand drop breakup dynamics when phase change is absent [43–47], however, the interaction between drop deformation/breakup and vaporization is not fully understood. In practical spray applications, due to the large geometric scale and the huge number of drops involved, it is inivable to resolve the interface of each individual drop. For those macro-scale simulations, the Euler-Lagrange point-particle simulations are typically used [48–51]. Since the drop-scale interfacial and flow physics are not resolved, the mass and energy transfer between the drop and the surrounding gas

must be represented by sub-grid models, similar to the drag model for momentum transfer [52,53]. The conventional models to predict drop vaporization are empirical correlations for spherical drops [54] and they will be invalid for drops with a Weber number close to or larger than the critical Weber number [43]. Models that can accurately predict the vaporization rate of drops undergoing significant deformation and even breakup remain to be established. High-fidelity interface-resolved simulations enabled by the present study will play an essential role in the development of such models.

The present method is implemented in the open-source solver *Basilisk* [55–57]. Validation tests and simulations are then performed using the modified *Basilisk* code. The key advantage of *Basilisk* is that it provides an infrastructure for octree/quadtrees mesh for spatial discretization, which allows an important capability to adapt the mesh in user-defined regions. This adaptive mesh refinement (AMR) feature is crucial for the efficient simulation of interfacial multiphase flows with vaporization. A VOF model with phase change on a quad-tree mesh has been implemented by Wang and Yang [32] in the *Gerris* code, the predecessor to *Basilisk*. One key difference between the two codes is on the parallelization of the adaptive mesh [55,57]. While *Gerris* uses a domain decomposition, *Basilisk* decomposes the tree directly and thus achieves improved parallel performance for large-scale simulations using a large number of processors and refinement levels. Due to the limitation of the *Gerris* code, the VOF model of Wang and Yang [32] was only tested with 2D simulations of drop vaporization. The two very recent works mentioned above by Gao et al. [39] and Zhao et al. [40] have also built a phase-change model on the *Basilisk* solver. The present method distinguishes itself from the previous studies by the following essential features. First, the present method has used a consistent approach to advect VOF (mass), momentum, and energy across the interface. This consistency between mass and momentum advection has been shown to be important for interfacial multiphase flows with large-density contrast [58]. The consistency among mass, momentum, and energy is also shown to be important to get accurate pressure and velocity across the interface for compressible flows [59]. Second, we have proposed a novel treatment to handle the vaporization-induced volumetric source, by which the VOF represented interfaces can be advected accurately and the Stefan flow in the gas phase can be rigorously captured. This treatment will not require an additional velocity field and solving an additional Poisson equation, as needed in the previous methods [35,36,40] and thus is more efficient and easy to implement. The present method carries a similar spirit to the method of Hardt and Wondra (HW) [25], which was adopted by Gao et al. [39] and others [32,60]. We also distribute the source to cells near the interface but not at the interfacial cells to preserve the correct velocity at the interfacial cells for VOF advection. In the HW method, a diffusion equation is required and the source is distributed to both gas and liquid cells. In contrast, we account only for the contribution of the volumetric source that is induced by density differences between the vapor and liquid, which is responsible for the introduction of the Stefan flow, and only distribute the source to a compact layer of pure gas cells near the interface in a mass-conservative way.

The rest of the paper is organized as follows. The physical model will be presented in Section 2. The numerical methods are then introduced in Section 3. The overall simulation approaches are validated through a series of tests in Section 4. We first start with the classic 1D Stefan and sucking problems (Sections 4.1 and 4.2), then we move on to the 3D bubble growth in superheated liquid (Section 4.3). For these cases, analytical solutions are available to validate the simulation results. Furthermore, we have simulated more realistic cases such as film boiling (Section 4.4) and vaporization of a moving drop in a high-temperature environment (Section 5.1). The simulation results were then compared against former numerical and experimental studies. Finally, a large-scale simulation of the aerobreakup of a vaporizing drop has been performed to demonstrate the capability of the present method in resolving complex interfacial multiphase flows with vaporization (Section 5.2).

2. Multiphase models and governing equations

In the present study, a simulation framework for liquid–gas two-phase flows with phase change is developed. For the velocity field, the two phases are considered as “one fluid” and share the same velocity field. The momentum conservation equation for both phases is

$$\rho \left(\frac{\partial \mathbf{u}}{\partial t} + \mathbf{u} \cdot \nabla \mathbf{u} \right) = -\nabla p + \nabla \cdot (2\mu \mathbf{D}) + \rho \mathbf{g} + \sigma \kappa \delta_\gamma \mathbf{n}_\gamma \quad (1)$$

where \mathbf{u} , p , μ , ρ , σ , and κ are the velocity, pressure, dynamic viscosity, density, surface tension coefficient, and interfacial curvature, respectively. The interface normal is denoted by \mathbf{n}_γ , where the subscript γ indicates properties associated with the interface. The surface tension is a singular force localized on the sharp interface using the Dirac distribution function δ_γ . The deformation tensor is defined as $\mathbf{D} = (\nabla \mathbf{u} + \nabla \mathbf{u}^T)/2$. Gravity, which can be easily included, is neglected in the cases considered in the present paper.

The two different phases are distinguished by the color function c , which follows the advection equation,

$$\frac{\partial c}{\partial t} + \mathbf{u} \cdot \nabla c = \frac{-s_\gamma}{\rho_l} \quad (2)$$

It is taken that $c = 1$ and 0 for liquid and gas phases, respectively. Therefore, the volume-averaged color function in a control volume is equivalent to the liquid volume fraction. The density and viscosity are calculated based on the liquid volume fraction using the arithmetic mean:

$$\rho = c\rho_l + (1 - c)\rho_g, \quad (3)$$

$$\mu = c\mu_l + (1 - c)\mu_g. \quad (4)$$

The volumetric source term (s_γ) on the right-hand side is associated with phase change. The phase change will also modify the continuity equation as

$$\nabla \cdot \mathbf{u} = s_\gamma \left(\frac{1}{\rho_g} - \frac{1}{\rho_l} \right), \quad (5)$$

where the subscripts l and g denote the liquid and gas properties, and the velocity field is divergence-free only in the region away from the interface. As will be discussed in the later section, the projection method is employed and as a result, the pressure Poisson equation will be solved to guarantee the projected velocity satisfies the continuity equation. Furthermore, we will distribute the volumetric source at the interface s_γ to adjacent pure gas cells, and the discretized distributed volumetric source is denoted by \hat{s} .

The volumetric source term (s_γ) depends on the rate of vaporization (j_γ) and the interfacial area density (ϕ_γ),

$$s_\gamma = j_\gamma \phi_\gamma. \quad (6)$$

The rate of phase change (j_γ) is determined based on the heat fluxes from both sides of the interface,

$$j_\gamma = \frac{1}{h_{l,g}} (k_l(\nabla T_l)_\gamma \cdot \mathbf{n}_\gamma - k_g(\nabla T_g)_\gamma \cdot \mathbf{n}_\gamma) \quad (7)$$

where T , k , and $h_{l,g}$ are the temperature, thermal conductivity, and latent heat, respectively. Note that the rate of phase change here is governed by the temperature gradient, instead of the vapor concentration gradient [17,18]. For the expression given here, $j_\gamma > 0$ for vaporization and $j_\gamma < 0$ for condensation.

The energy (temperature) equations in the gas and liquid regions are [27,35,36],

$$\rho_g C_{p,g} \left(\frac{\partial T_g}{\partial t} + \mathbf{u} \cdot \nabla T_g \right) = \nabla \cdot (k_g \nabla T_g), \quad (8)$$

$$\rho_l C_{p,l} \left(\frac{\partial T_l}{\partial t} + \mathbf{u} \cdot \nabla T_l \right) = \nabla \cdot (k_l \nabla T_l) \quad (9)$$

with the Dirichlet boundary condition at the vaporizing interface $(T_g)_\gamma = (T_l)_\gamma = T_{sat}$. The isobaric specific heat for gas and liquid are

denoted by $C_{p,g}$ and $C_{p,l}$, respectively. Keeping the two temperature fields makes it easier to apply the temperature boundary condition at the interface. It is worth noting that there are no additional source terms in the energy equations due to phase change since it has been implicitly accounted for by the boundary condition at the interface.

3. Numerical methods

The governing equations are solved using a finite volume approach based on the projection method. The advection of the color function is solved using a geometric VOF method [61]. The advection of momentum near the interface is conducted in a manner consistent with the VOF advection [58,62]. The surface tension term in the momentum equation is discretized using the balanced-force continuum-surface-force method [63]. The height-function method is used for curvature calculation [56]. A staggered-in-time discretization of the volume-fraction/density and pressure leads to a formally second-order accurate time discretization. The quadtree/octree mesh is used to discretize the 2D/3D spatial domains, providing important flexibility to dynamically refine the mesh in user-defined regions. The adaptation criterion is based on the wavelet estimate of the discretization errors of the user-defined variables [64]. Since the present study is focused on the new development for the inclusion of phase change, the above methods will be briefly reviewed below (Sections 3.1, 3.2). The detailed implementation of the methods without phase change can be found in previous studies [56,58].

To include vaporization in the numerical model, we need to solve the energy equations for both phases to obtain the temperature near the interface (Section 3.3). Then based on the temperature gradients on both sides of the interface, the vaporization rate is estimated (Section 3.4). Furthermore, the interface recession due to the reduction in liquid volume (referred to as interface shifting) needs to be accounted for by modifying the VOF field (Section 3.5). Finally, the additional volumetric source due to phase change will be added to the pressure equation to account for the non-zero divergence for the velocity near the interface and the resulting Stefan flow due to the expansion of the dense liquid into a gaseous state (Section 3.6). A new treatment is proposed to handle the volumetric source to guarantee that the velocity at the interface is correctly represented and can be directly used in VOF advection. These procedures will be described below in sequence.

3.1. VOF method

The advection equation for the color function, Eq. (2), is solved using a geometric VOF method. The interface in each computational cell is reconstructed as a planar surface based on the cell-average color function (liquid volume fraction). The interface normal \mathbf{n}_γ is computed based on the Mixed Youngs-Centred (MYC) method [65]. The detailed implementation of the method on an octree mesh was given by Popinet [56]. Eq. (2) can be rewritten in conservative form as

$$\frac{\partial c}{\partial t} = -\nabla \cdot (c\mathbf{u}) + c_e \nabla \cdot \mathbf{u} + \frac{-s_\gamma}{\rho_l} \quad (10)$$

where the first two terms on the right-hand side are for the regular VOF method without phase change, while the last term represents the additional shift of interface due to phase change, the discussion of which will be given later in Section 3.5. The VOF advection is conducted in a direction-split manner, taking a 2D example,

$$\frac{c_{i,j}^* - c_{i,j}^n}{\Delta t} = -\frac{F_{c,i+1/2,j} - F_{c,i-1/2,j}}{\Delta V} + \left(c_c \frac{\partial u}{\partial x} \right)_{i,j}, \quad (11)$$

$$\frac{c_{i,j}^{n+1} - c_{i,j}^*}{\Delta t} = -\frac{G_{c,i,j+1/2} - G_{c,i,j-1/2}}{\Delta V} + \left(c_c \frac{\partial v}{\partial y} \right)_{i,j}, \quad (12)$$

where ΔV is the cell volume, and the superscript c^* denotes the auxiliary color-function. The value of the color function at the cell

center is denoted by c_c , which is taken to be $c_c = 1$ if $c > 0.5$ and 0 if $c < 0.5$. It was proved by Weymouth and Yue [61] that the value of c_c must be kept as a constant for all sweep directions to achieve exact mass conservation. The VOF fluxes in x and y directions are denoted as F_c and G_c , respectively. The flux on the right surface in x direction, $F_{c,i+1/2,j}$, is calculated as

$$F_{c,i+1/2,j} = c_a u_{f,i+1/2,j} S, \quad (13)$$

where $u_{f,i+1/2,j}$ is the u-velocity at the cell surface and S is the surface area. The volume fraction of liquid that is advected across the cell surface over Δt is c_a , which is calculated based on the reconstruction of the interface. The VOF fluxes in the other directions are calculated similarly.

3.2. VOF-consistent momentum advection

It is important to advect the momentum across the interface consistently with the VOF (mass) advection, as shown in previous studies [58, 66, 67]. To make the advection of momentum and mass consistent, the momentum for the liquid and gas phases are handled separately:

$$\frac{(c\rho_l\mathbf{u})^a - (c\rho_l\mathbf{u})^n}{\Delta t} = -\nabla \cdot (c\rho_l\mathbf{u}\mathbf{u}) + (c\rho_l\mathbf{u})_c \nabla \cdot \mathbf{u}, \quad (14)$$

$$\frac{((1-c)\rho_g\mathbf{u})^a - ((1-c)\rho_g\mathbf{u})^n}{\Delta t} = -\nabla \cdot ((1-c)\rho_g\mathbf{u}\mathbf{u}) + ((1-c)\rho_g\mathbf{u})_c \nabla \cdot \mathbf{u}, \quad (15)$$

where the superscript a denotes the auxiliary variables accounting only for the advection term. The momentum is advected as a tracer associated with VOF advection non-diffusely [68]. The momentum flux for each phase is computed as the product the VOF flux for the corresponding phase and the momentum per unit volume to be advected [58]. Taking the x-momentum for the liquid phase as an example,

$$\frac{(c\rho_l\mathbf{u})_{i,j}^* - (c\rho_l\mathbf{u})_{i,j}^n}{\Delta t} = -\frac{F_{u,i+1/2,j} - F_{u,i-1/2,j}}{\Delta V} + \left((c\rho_l\mathbf{u})_c \frac{\partial u}{\partial x} \right)_{i,j}, \quad (16)$$

$$\frac{(c\rho_l\mathbf{u})_{i,j}^a - (c\rho_l\mathbf{u})_{i,j}^*}{\Delta t} = -\frac{G_{u,i,j+1/2} - G_{u,i,j-1/2}}{\Delta V} + \left((c\rho_l\mathbf{u})_c \frac{\partial v}{\partial y} \right)_{i,j}, \quad (17)$$

where F_u and G_u denote the x-momentum fluxes for in x and y directions. The x-momentum flux on the right surface of the cell is calculated as

$$F_{u,i+1/2,j} = (\rho_l u)_a F_{c,i+1/2,j}, \quad (18)$$

where $(\rho_l u)_a$ is the momentum per unit volume to be advected. The Bell-Collela-Glaz (BCG) second-order upwind scheme [69] is used for the reconstruction of $(\rho_l u)_a$ in the upwind cell of the surface where the flux is to be evaluated. The generalized minmod slope limiter is employed to compute the gradient. The liquid momentum $(c\rho_l\mathbf{u})_c$ at the cell center is the analog of c_c , and $(c\rho_l\mathbf{u})_c = c\rho_l u$ if $c > 0.5$ and 0 if $c < 0.5$. After the advection of momentum in all directions, the unified velocity is obtained by

$$\mathbf{u}_{i,j}^a = \frac{(c\rho_l\mathbf{u})_{i,j}^a + ((1-c)\rho_g\mathbf{u})_{i,j}^a}{(c\rho_l\mathbf{u})_{i,j}^a + ((1-c)\rho_g\mathbf{u})_{i,j}^a}. \quad (19)$$

3.3. Energy equations and consistent energy advection

The energy equations for both phases, i.e., Eqs. (8)–(9), are solved with the Dirichlet boundary condition at the vaporizing interface $(T_g)_\gamma = (T_l)_\gamma = T_{sat}$. The boundary conditions at the interfaces are invoked by setting $T_g = T_{sat}$ in the cells with $f > 0$ and $T_l = T_{sat}$ in cells with $f < 1$ [70]. Note that more sophisticated immersed Dirichlet boundary conditions have been proposed recently [39, 40]. Nevertheless, the simple treatment here seems to be sufficient to yield accurate results.

The energy fluxes for the advection terms, e.g., $\mathbf{u} \cdot \nabla(\rho_l C_{p,l} T_l)$, are computed similarly to the momentum fluxes discussed previously, namely the energy is advected as a tracer associated with the VOF advection. In such a way, the numerical diffusion across the interface can be avoided when we advect energy across the interface. Furthermore, the advection methods for mass, momentum, and energy across the interface are consistent. The consistent advection approach is similar to the methods of Zhang et al. [59] for compressible interfacial multiphase flows and thus will make the future extension of the present methods toward compressible flows easier. The energy to be advected in the upwind cell is computed based on the linear reconstruction of the variable using the Bell–Colella–Glaz scheme and the minmod slope limiter [55, 69].

The time integration of the diffusion terms is treated fully implicitly. When the temperature for the vapor and liquid are lower than T_{sat} , there will be no vaporization, since here we neglect the evaporation effect due to the gradient of vapor concentration. There will be no need to make any adjustments to the interfacial temperature. Nevertheless, as the temperature on either side of the interface increases to be over the saturation temperature, which is the scenario of interest in the present study, vaporization will occur. In such a case, the vapor is assumed to be saturated at the interface, and the temperature at the interface is taken to be fixed at the saturation temperature, T_{sat} . The heat sink due to the latent heat of vaporization is implicitly included. The interfacial temperature is then used as the boundary condition for solving the diffusion term in each phase. In all the tests considered in the present study, the interfaces are always saturated.

A potential improvement for spatial discretization of the diffusion term is to consider a sub-grid embedded boundary condition for the interface temperature [35, 36, 39, 40]. Nevertheless, the present methods already yield very accurate predictions as shown later in the validation studies (Section 4). Additionally, previous studies using embedded boundary models for the interface have shown artificial velocity fluctuations near the interface [39]. This is likely due to the use of the VOF interface normal to compute the interfacial temperature gradient: even in simple interface advection cases, the direction of the interface normal in cells exhibits fluctuations between time steps. The fluctuations in the interface normal will result in fluctuations in the computed interfacial temperature gradient and, eventually, the rate of vaporization. Therefore, if one wants to take advantage of the sub-grid interfacial location, this challenge must be carefully tackled, and such an extension will be relegated to future works.

3.4. Calculation of vaporization rate

The vaporization rate j_γ is computed in every interfacial cell ($1 > c > 0$). The determination of j_γ (Eq. (7)) requires the temperature gradient on both the liquid and gas sides of the interface: $(\nabla T_l)_\gamma$ and $(\nabla T_g)_\gamma$. The calculations for the gas and liquid sides are similar. Here we take the gas temperature gradient as an example to demonstrate the procedures. First of all, it is assumed that the temperature gradient is aligned with the interface normal near the interface, therefore, the projection of the temperature gradient to the interface normal is approximated by its magnitude, i.e., $(\nabla T_g)_\gamma \cdot \mathbf{n}_\gamma \approx \|(\nabla T_g)_\gamma\|$, where $\|\cdot\|$ denotes the magnitude of a vector. The magnitude of the gas temperature gradient at the interface is then obtained by extrapolation from the neighboring pure gas cells ($c = 0$). Considering the interfacial cell \hat{i}, \hat{j} in a 2D 5×5 stencil, in which the temperature gradient is approximated as

$$\|(\nabla T_g)_\gamma\| = \|(\nabla T_g)_{\hat{i},\hat{j}}\| = \sum_{i=\hat{i}-2,j=\hat{j}-2}^{i=\hat{i}+2,j=\hat{j}+2} \hat{w}_{i,j} \|(\nabla T_g)_{i,j}\|, \quad (20)$$

where the normalized weight $w_{i,j}$ for a cell i, j in the stencil is computed as

$$\hat{w}_{i,j} = \frac{w_{i,j}}{\sum_{i=\hat{i}-2,j=\hat{j}-2}^{i=\hat{i}+2,j=\hat{j}+2} w_{i,j}}, \quad (21)$$

where

$$w_{i,j} = \begin{cases} \xi_{i,j} \|\mathbf{d}_{i,j}\|^2, & \text{if } c = 0 \\ 0, & \text{if } c > 0. \end{cases} \quad (22)$$

In interfacial and liquid cells, $w_{i,j} = 0$, and in pure gas cells $w_{i,j}$ is associated with the distance vector from the center of the pure gas cell to the center of the interfacial cell, i.e., $\mathbf{d}_{i,j} = \mathbf{x}_{i,j} - \mathbf{x}_{i,j}$, and its projection to the interfacial normal direction, i.e., $\xi_{i,j} = |\mathbf{n}_\gamma \cdot \mathbf{d}_{i,j}|$, see Fig. 1(c). The central difference approximation is used to calculate the temperature gradient, we have used only the pure gas cells to avoid computing the temperature gradient across the interface. The large stencil used here is to make sure at least one pure gas cell can be found. As a result, the primary contributions to the temperature gradient at the interfacial cell are taken from the pure gas cells where the central difference can be used without the temperature from the interfacial cells, see Fig. 1(c). Note that the same procedure applies to the temperature gradient on the liquid side $\|(\nabla T_l)_\gamma\|$.

With the gas and liquid temperature gradients in the interfacial cell, the rate of vaporization for an interfacial cell can be computed according to Eq. (7). The volumetric source in the interfacial cell due to phase change s_γ is then computed using Eq. (6). Note that the interfacial area density in an interfacial cell is evaluated by $\phi_\gamma = A_\gamma / \Delta V$, where A_γ is the area of the VOF reconstructed interface in the cell.

3.5. Vaporization-induced interface shifting

The contribution of vaporization on the liquid phase results in an additional shift of the interface toward the liquid side. The vaporization-induced interfacial velocity \mathbf{u}_γ is normal to the interface, namely $\mathbf{u}_\gamma = u_\gamma \mathbf{n}_\gamma$, see Fig. 1(b) [36], where u_γ is expressed as

$$u_\gamma = -\frac{j_\gamma}{\rho_l}. \quad (23)$$

and the negative sign indicates the direction is the opposite of the interface normal. The interface shifting is handled explicitly by shifting the reconstructed VOF interface by the distance over one time step as

$$\Delta d_\gamma = -\frac{j_\gamma}{\rho_l} \Delta t. \quad (24)$$

The volume fraction of the interfacial cell c is then updated based on the shifted interface. Occasionally, the interface may leave the current cell if the liquid volume fraction is very small in the previous time step. In such a case, the interface moves to a neighboring pure liquid cell. Then that liquid cell will become an interfacial cell, with the liquid volume fraction computed based on the interface location. Since phase change induces a new velocity scale u_γ , it is accounted for in the CFL condition for the time step calculation.

3.6. Pressure equations and volumetric-source distribution

When the higher-density liquid turns into lower-density vapor, the Stefan flow is introduced in the gas phase and the Stefan flow velocity is

$$u_{st} = j_\gamma \left(\frac{1}{\rho_g} - \frac{1}{\rho_l} \right) \quad (25)$$

This production of volume due to the different densities is represented by the divergence source term in the continuity Eq. (5). Since in the projection method the continuity equation is incorporated by solving the pressure Poisson equation, an additional source term appears in the Poisson equation.

The velocity jump across the interface creates a challenge in advecting the color function using the VOF method [36,39,40]. When phase change is absent, the gas and liquid velocities are the same in the interfacial cell, and the velocity for the interfacial cell is ready to be used to compute the VOF fluxes and to advect the interface. However,

when the phase change occurs, the gas and liquid velocities jump across the interface. As a result, the velocity in the interfacial cell, which is generally biased towards the gas/vapor velocity, is *not* the correct velocity of the interface. One way to overcome this issue is to solve an additional Poisson equation to extrapolate the liquid velocity across the interface [35,36,39]. This treatment will result in a divergence-free liquid velocity at the interface for VOF advection and yield accurate results for the vaporizing interface. However, this approach requires an additional Poisson equation, which increases the computational expense. In the method of Malan et al. [36], the boundary conditions on the two artificial embedded boundaries on both sides of the interface are specified to solve the Poisson equation. For moving or deforming interfaces, these embedded boundary conditions need to be imposed every time step, which further increases the computational cost and algorithm complexity, in particular for adaptive octree mesh.

In the present study, we propose a simple yet accurate method to resolve this numerical challenge in obtaining the current interface advection velocity when phase change is present. The volumetric source due to vaporization s_γ is first calculated according to the steps described in Section 3.4, based on the temperature gradients for gas and liquid in the interfacial cells. Then instead of applying the volumetric source s_γ right at the interfacial cell, we distribute the volumetric source to the nearest pure gas cells in a 5^3 stencil in 3D (5^2 in 2D). The distribution of the volumetric source from the interfacial cell (\hat{i}, \hat{j}) to a pure gas cell (i, j) in the stencil ($\hat{i}-2 \leq i \leq \hat{i}+2$ and $\hat{j}-2 \leq j \leq \hat{j}+2$) is

$$(\hat{s}_{i,j})_{\hat{i},\hat{j}} = \hat{m}_{i,j}(s_\gamma)_{\hat{i},\hat{j}}, \quad (26)$$

where $\hat{m}_{i,j}$ is the normalized weight and is defined similarly to Eq. (21) as

$$\hat{m}_{i,j} = \frac{m_{i,j}}{\sum_{i=\hat{i}-2, j=\hat{j}-2}^{i=\hat{i}+2, j=\hat{j}+2} m_{i,j}}, \quad (27)$$

where

$$m_{i,j} = \begin{cases} \xi_a / \|\mathbf{d}_{i,j}\|, & \text{if } c = 0 \\ 0, & \text{if } c > 0. \end{cases} \quad (28)$$

As a result, only pure gas cells in the stencil will receive a distribution. The weight for a gas cell is related to the ratio between the projection of the distance vector $\mathbf{d}_{i,j} = \mathbf{x}_{i,j} - \mathbf{x}_{i,j}$ to the interfacial normal direction, i.e., $\xi_{i,j} = |\mathbf{n}_\gamma \cdot \mathbf{d}_{i,j}|$, and the norm of $\mathbf{d}_{i,j}$. The gas cell in the stencil that is more aligned with the interface normal will thus receive a bigger distribution.

Note that the distributed volumetric source in a pure gas cell, \hat{s} , is the sum of the source distribution from all the nearby interfacial cells. The integration of the distributed source \hat{s} in all pure gas cells is equal to the integration of the volumetric source s_γ over all the interfacial cells,

$$\sum_{1>c_{i,j}>0} (s_\gamma)_{i,j} = \sum_{c_{i,j}=0} \hat{s}_{i,j} \quad (29)$$

ensuring the conservation of the generated vapor volume from the whole interface. Note that here we have used the 2D case to explain the algorithm, and the algorithm is very similar for 3D cases.

Finally, the distributed source is added to the pressure Poisson equation as

$$\nabla \cdot \left(\frac{\Delta t}{\rho} \nabla p \right) = \nabla \cdot \mathbf{u}^{**} - \hat{s} \left(\frac{1}{\rho_g} - \frac{1}{\rho_l} \right), \quad (30)$$

where \mathbf{u}^{**} is the auxiliary velocity that accounts for all the terms in the momentum equation except the pressure term.

There are several important advantages for the present treatment of the vaporization-induced volumetric source. First of all, by donating the volumetric source from the interfacial to the neighboring gas cells, the velocity in the interfacial cell will not be “contaminated” by the Stefan flow and will remain as the liquid velocity by which the interface moves

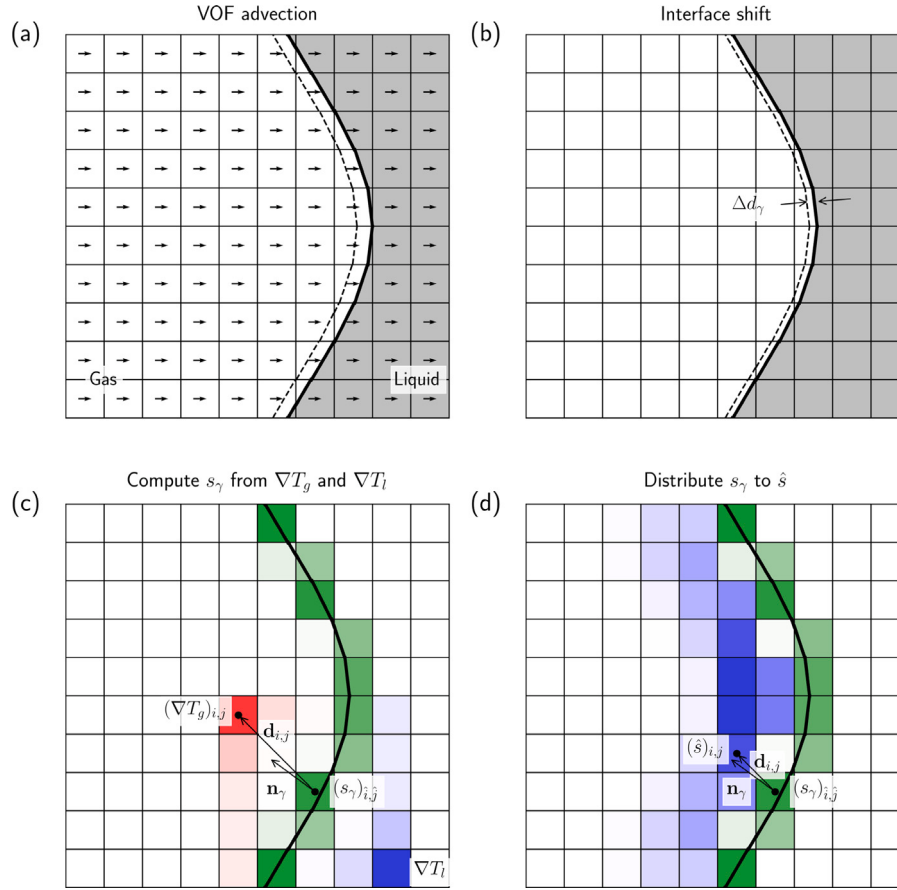


Fig. 1. Key steps of the VOF advection with phase change. (a) the VOF advection based on the liquid velocity, (b) shifting the interface by Δd_γ , (c) computing the vaporization source term s_γ , and (d) distributing the s_γ to \hat{s} in the near-by pure gas cells.

(before we impose the additional shifting discussed in Section 3.5). Furthermore, the distributed volumetric source in the pure gas cells will induce the Stefan flow in the gas region near the interface. As a numerical approximation, we have moved the volumetric source away from the interface, which will slightly modify the Stefan flow right next to the interface. However, since the relocation distance for s_γ to the neighboring cell is typically less than two grid cells, its influence is very small, as will be shown later in the test results (Section 4).

The present method also distinguishes itself from the source term distribution method by Hardt and Wondra (HW) [25,39] in several important aspects. At first, the present method does not need to solve an additional diffusion equation as required in the HW method. The direct distribution of the source in a compact stencil is beneficial in keeping the effective thickness of the volumetric source small. In general, we have used a 5^3 stencil centered at the interfacial cell, therefore, the effective thickness is about two cells. It is also possible to use a more compact 3^3 stencil; however, it will be less robust when there is a large distortion of the interface and there will be no pure gas cells present in the stencil. It is also worth noting that the present method assumes the vapor region is reasonably well resolved and there is at least one pure gas cell in the stencil. Secondly, in the Hardt and Wondra (HW) method the source is distributed in both pure gas and liquid cells as s_γ/ρ_g and s_γ/ρ_l , respectively, the present method only distributes the volumetric source due to density difference, $s_\gamma(1/\rho_g - 1/\rho_l)$, in the pure gas cells and the disappearance of mass in the liquid side is accounted for by shifting the VOF-represented interface explicitly (see Section 3.5). While both methods will capture the Stefan flow and interface motion, the present method only needs to modify the velocity field on the gas side and thus has a more compact region of the source distribution. It is worth noting that, vaporization will only modify the velocity and pressure fields

and will induce the Stefan flow when the densities of the two phases are different (see Eqs. (5) and (30)). The Stefan flow only appears in the lighter gas phase ($\rho_g \ll \rho_l$), therefore, distributing the volumetric source only in the gas phase is more consistent with the vaporizing flow physics.

3.7. Staggered-in-time temporal discretization

The above spatially discrete equations are temporally discretized using the second-order staggered-in-time method in the *Basisk* solver [56]. The temporally discrete equations are given below, which can be combined with the spatial discretization discussed above to achieve the fully discrete equations.

- Advection equation

$$\frac{c^{n+\frac{1}{2}} - c^{n-\frac{1}{2}}}{\Delta t} = -\nabla \cdot (c^n \mathbf{u}^n) + c_c^n \nabla \cdot \mathbf{u}^n + \left(\frac{-s_\gamma}{\rho_l} \right)^{n-\frac{1}{2}} \quad (31)$$

- Momentum equation - prediction step

$$\frac{(\rho_l c \mathbf{u})^* - (\rho_l c \mathbf{u})^n}{\Delta t} = -\mathbf{u}^n \cdot \nabla (\rho_l \mathbf{u})^n, \quad (32)$$

$$\frac{(\rho_g(1-c)\mathbf{u})^* - (\rho_g(1-c)\mathbf{u})^n}{\Delta t} = -\mathbf{u}^n \cdot \nabla (\rho_g \mathbf{u})^n, \quad (33)$$

$$\mathbf{u}^* = \frac{(\rho_l c \mathbf{u})^* + (\rho_g(1-c)\mathbf{u})^*}{\rho_l c^{n+1/2} + \rho_g(1-c^{n+1/2})} \quad (34)$$

$$\rho^{n+\frac{1}{2}} \frac{\mathbf{u}^{**} - \mathbf{u}^*}{\Delta t} - \nabla \cdot \left(\mu^{n+\frac{1}{2}} \mathbf{D}^{**} \right) = \nabla \cdot \left(\mu^{n+\frac{1}{2}} \mathbf{D}^* \right) + (\sigma \kappa \delta_\gamma \mathbf{n}_\gamma)^{n+\frac{1}{2}} \quad (35)$$

- Pressure Poisson equation

$$\nabla \cdot \left(\frac{\Delta t}{\rho^{n+\frac{1}{2}}} \nabla p^{n+\frac{1}{2}} \right) = \nabla \cdot \mathbf{u}^{**} - \left(\hat{s} \left(\frac{1}{\rho_g} - \frac{1}{\rho_l} \right) \right)^{n+\frac{1}{2}} \quad (36)$$

- Momentum equation - projection step

$$\mathbf{u}^{n+1} = \mathbf{u}^{**} - \frac{\Delta t}{\rho^{n+\frac{1}{2}}} \nabla p^{n+\frac{1}{2}} \quad (37)$$

- Energy equation

$$\frac{(\rho_l C_{p,l} T_l)^{n+\frac{1}{2}} - (\rho_l C_{p,l} T_l)^{n-\frac{1}{2}}}{\Delta t} = -\mathbf{u}^n \cdot \nabla (\rho_l C_{p,l} T_l)^n + \nabla \cdot (k_l \nabla T_l)^{n+\frac{1}{2}} \quad (38)$$

$$\frac{(\rho_g C_{p,g} T_g)^{n+\frac{1}{2}} - (\rho_g C_{p,g} T_g)^{n-\frac{1}{2}}}{\Delta t} = -\mathbf{u}^n \cdot \nabla (\rho_g C_{p,g} T_g)^n + \nabla \cdot (k \nabla T_g)^{n+\frac{1}{2}} \quad (39)$$

Finally, the overall solution steps are summarized in Algorithm 1.

Algorithm 1 Full algorithm summary

```

Initialization of  $f$ ,  $\mathbf{u}$ ,  $T_l$ ,  $T_g$ 
while  $t < t_{end}$  do
    Calculate  $\Delta t$  based on CFL constraint
    VOF reconstruction;
    VOF advection neglecting the source term due to phase change
    (Eqs. (11), (12), (31));
    VOF-consistent advection of momentum and energy (Eqs. (32)-
    (34) and Eqs. (38)-(39))
    Solve diffusion terms in energy equations to obtain  $T_l^{n+\frac{1}{2}}$  and
     $T_g^{n+\frac{1}{2}}$  (Eqs. (38)-(39))
    Compute the volumetric source term  $s_\gamma$  (Eqs. (6)-(7) and
    (20)-(21))
    Shift reconstructed interface by  $\Delta d_\gamma$  (Eq. (24)) to account for the
    phase-change term in the advection equation (Eq. (31))
    Distribute  $s_\gamma$  to neighboring pure gas cells and compute  $\hat{s}$ 
    Solve diffusion term in momentum equation to obtain  $\mathbf{u}^{**}$ 
    (Eq. (35))
    Compute  $p^{n+\frac{1}{2}}$  by solving the Poisson Eq. (36)
    Correct  $\mathbf{u}^{n+1}$  by projection (Eq. (37))
end while

```

3.8. Quadtree/octree mesh

The physical models and numerical methods described above have been implemented in the *Basilisk* code using adaptive octree/quadtrees meshes. The maximum level of refinement L can be compared with a fixed grid resolution of 2^L cells in each coordinate direction; i.e., L_9 corresponds to $2^9 = 512$ cells in the x direction or 512^3 cells in 3D. Note that the finite volume cells have equal dimensions (square in 2D or cubic 3D), i.e., $\Delta x_{min} = \Delta y_{min}$. The mesh adaptation algorithm is based on a wavelet-estimated discretization error [57,64], where the refinement criteria are based on temperature (T), volume fraction (c), and velocity (\mathbf{u}). The advantage of using an adaptive mesh is that a higher grid resolution is only used in the user-defined regions; i.e., near the interface, so that the total number of computational cells can be significantly reduced. To maintain the simplicity in the interface temperature gradient calculation (Section 3.4) and s_γ distribution (Section 3.6), the mesh near the interface is always refined to the maximum level (5 cells on either side of the interface). This is achieved by refining the mesh based on a level-set function. The addition to the computational cost for this treatment is minor because the temperature

Table 1

Summary of the validation cases considered in the present paper.

| Case | Section | Purpose |
|-----------------|---------|---|
| Stefan Problem | 4.1 | Vaporization due to heated gas |
| Sucking problem | 4.2 | Vaporization due to heated liquid |
| Bubble growth | 4.3 | 3D interface motion due to vaporization |
| Film boiling | 4.4 | Complex deformation of vaporizing interface |

gradient is typically large near the interface and requires the maximum level of grid refinement.

The *Basilisk* code has different parallelization options. In this study, we have used parallelization based on tree decomposition and MPI [57]. As a result, the computational domain is split into blocks with irregular shapes, instead of simple boxes as in conventional domain decomposition. This advanced parallelization technique guarantees good performance for large-scale simulations using a large number of processors and refinement levels. When an interfacial cell is located at the block boundary, the procedures for the distribution of the volumetric source (Section 3.6) and the shifting of the interface (Section 3.5) involve the modification of variables in the ghost cells of an MPI block. An additional MPI communication is thus required for block boundary with interfacial cells. Nevertheless, the computational cost is small compared to that for regular communications between blocks.

4. Validation

To validate the present methods and their implementation in the *Basilisk* code, a series of test cases were performed, see Table 1. The purpose of each test is also listed. The CFL number is set to 0.2 for all cases. The two new velocities induced by vaporization, i.e., the Stefan flow velocity (Eq. (25)) and the vaporization-induced interface shifting velocity u_γ (Eq. (23)) are also accounted for in the calculation of the time step.

4.1. 1D Stefan problem

The 1D Stefan problem is a common test case [18,24,25,27,35,36,39]. The domain consists of a vapor region next to a heated wall and a liquid region, see Fig. 2. The wall temperature, $T_w > T_{sat}$, is fixed. Initially, the liquid is at saturation temperature (T_{sat}). The liquid is vaporized at the interface due to the heat flux from the vapor. The vapor generated at the interface pushes the liquid to the right. The liquid will move out from the right edge of the domain, on which the pressure outlet boundary condition (BC) is imposed. The analytical solution for the temporal evolution of the interface position x_γ is given as

$$x_\gamma(t) = 2\beta\sqrt{\alpha_g t}, \quad (40)$$

where $\alpha_g = k_g/(\rho_g C_{p,g})$ is the gas thermal diffusivity and β is computed from the transcendental equation

$$\beta \exp(\beta^2) \operatorname{erf}(\beta) = \frac{C_{p,g}(T_w - T_{sat})}{h_{lg}\sqrt{\pi}}, \quad (41)$$

where $\operatorname{erf}()$ is the Gauss error function. The temperature in the vapor region, as a function of space and time, is given as

$$T_g(x, t) = T_w + \left(\frac{T_{sat} - T_w}{\operatorname{erf}(\beta)} \right) \operatorname{erf} \left(\frac{x}{2\sqrt{\alpha_g t}} \right). \quad (42)$$

Though the flow is 1D, simulations were performed on a 2D square domain with edge length $L_0 = 1$ mm, see Fig. 2. The exact solution at $t = 0.027$ s was used as the initial condition and the corresponding initial width of the vapor region is $H_0 = 0.1$ mm. The fluid is water and the properties are listed in Table 2. The wall temperature is $T_w = 383.15$ K. The simulation results are presented in Fig. 3 for three levels of grid refinement: $L5$, $L6$, and $L7$. It can be observed that the temporal

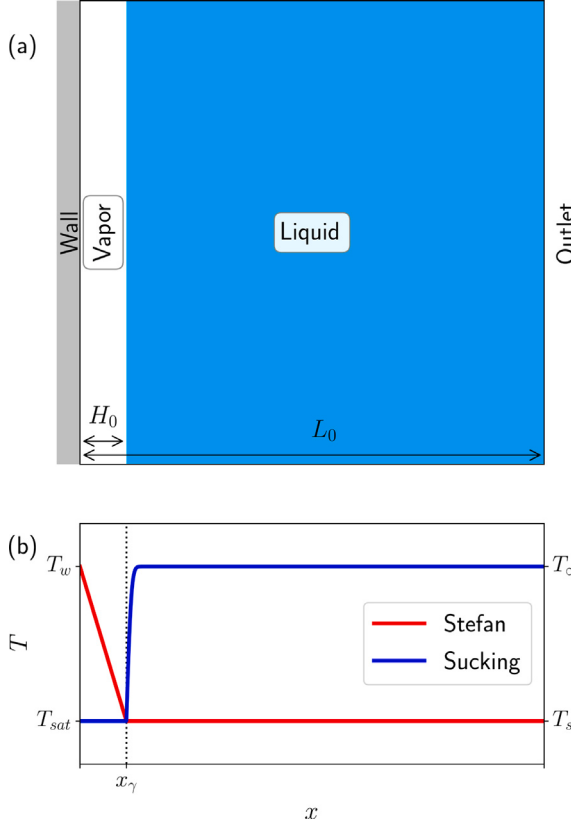


Fig. 2. Schematics for the 1D Stefan and sucking tests: (a) computational domain and (b) temperature distribution. Note that x_γ is the interface location.

evolution of the interface location for all three meshes matches very well with the analytical solution (see Fig. 3(a)). The simulations have been run to $t = 1.2$ s. The spatial distribution of temperature at the final time is shown in Fig. 3(b). Though we have solved T_g and T_l separately, here we plot the overall temperature T , which is defined as $T = T_g$ in vapor, $T = T_l$ in liquid, and $T = T_{\text{sat}}$ at the interface. It is clearly seen that the numerical results converge to the exact solution as the mesh is refined. It is also observed that the spatial variation of temperature in the vapor region is approximately linear. That is why even a coarse mesh is sufficient to yield a good approximation. Finally, the spatial variation of the u -velocity is shown in Fig. 3(c), compared with the exact solution. Ideally, the velocity in the vapor is zero and that in the liquid is constant in space, $u_l(t) = \dot{x}_\gamma$. Due to the distribution of the volumetric source to the pure gas cells, the numerical results show non-zero vapor velocity in a narrow region on the left of the interface. When the mesh is refined, the thickness of the non-zero velocity region reduces. It is worth noting that the liquid velocity is preserved to be constant on the right of the interface, which converges to the exact value as the cell size decreases. If the source is distributed to both the gas and liquid cells as in the HW method [39], numerical smearing will also appear in the liquid velocity.

4.2. 1D sucking problem

Another common validation case is the 1D sucking problem, also known as the boiling interface problem [18,24,27,35,40]. The temperature distribution is what differentiates this problem from the Stefan problem, see Fig. 2(b). Both the wall and vapor temperature are at the saturation temperature, i.e., $T_w = T_g = T_{\text{sat}}$, while the liquid is superheated and the liquid temperature at the right boundary of the domain, which is far from the interface, is fixed at T_∞ . The heat flux

Table 2

Properties of the saturated water (Section 4.1), Fluid A (Sections 4.2–4.3), and Fluid B 4.4.

| Property | Water | | Fluid A | | Fluid B | |
|---|--------|---------|---------|-------|---------|-------|
| | Liquid | Vapor | Liquid | Vapor | Liquid | Vapor |
| ρ [kg/m ³] | 958.4 | 0.597 | 2.5 | 0.25 | 200 | 5 |
| k [W m ⁻¹ K ⁻¹] | 0.679 | 0.025 | 0.07 | 0.007 | 1 | 1 |
| $C_{p,g}$ [J kg ⁻¹ K ⁻¹] | 4216 | 2030 | 2.5 | 1 | 200 | 200 |
| μ [Pa s] | 2.8e-4 | 1.26e-5 | 7e-3 | 7e-4 | 0.1 | 0.005 |
| h_{lg} [J kg ⁻¹] | 2.26e6 | – | 100 | – | 1e4 | – |
| T_{sat} [K] | 373.15 | – | 1 | – | 1 | – |
| σ [N m ⁻¹] | 0.0728 | – | 0.001 | – | 0.1 | – |

Table 3

The relative error of the interface position at the final time for the 1D sucking problem and the order of convergence \mathcal{O} .

| Maximum grid level | Final interface location | Relative error (%) | \mathcal{O} |
|--------------------|--------------------------|--------------------|---------------|
| $L6$ | 0.086 | 4.2 | – |
| $L7$ | 0.088 | 1.5 | 1.46 |
| $L8$ | 0.089 | 0.6 | 1.42 |

from the liquid to the interface results in vaporization. Similarly, the generated vapor pushes the liquid to the right. The analytical solution for the interface position has the identical expression as that for the Stefan problem, i.e., Eq. (40), though the parameter β is computed from a different transcendental equation

$$\exp(\beta^2) \operatorname{erf}(\beta) \left[\beta - \frac{(T_\infty - T_{\text{sat}}) C_{p,g} k_l \sqrt{\alpha_g} \exp\left(-\beta^2 \frac{\rho_g^2 \alpha_g}{\rho_l^2 \alpha_l}\right)}{h_{lg} k_g \sqrt{\pi \alpha_l} \operatorname{erfc}\left(\beta \frac{\rho_g \sqrt{\alpha_g}}{\rho_l \sqrt{\alpha_l}}\right)} \right] = 0. \quad (43)$$

The exact solution of the liquid temperature is given as

$$T_l(x, t) = T_\infty - \left(\frac{T_\infty - T_{\text{sat}}}{\operatorname{erfc} \beta \frac{\rho_g \sqrt{\alpha_g}}{\rho_l \sqrt{\alpha_l}}} \right) \operatorname{erfc} \left(\frac{x}{2\sqrt{\alpha_l t}} + \beta \frac{\rho_g - \rho_l}{\rho_l} \sqrt{\frac{\alpha_g}{\alpha_l}} \right). \quad (44)$$

In this test case, we have set $L_0 = 1$ m, $H_0 = 0.05$ m, and $T_\infty/T_{\text{sat}} = 3$. The fluid properties (Fluid A) are provided in Table 2. The exact solution at $t = 0.1$ s was used as the initial condition, and then the simulation was run to $t = 2.1$ s. The different meshes $L6$, $L7$, and $L8$ were used and the results are presented in Fig. 4. It is clearly shown that the numerical results converge toward the exact solution when the mesh is refined. The trajectory of the interface and final temperature profile for the mesh $L8$ match the exact solution very well. Different from the Stefan problem, the liquid temperature near the interface rises rapidly and non-linearly in x in the sucking problem. The interface positions at the final time ($t = 2.1$ s) for different meshes are provided in Table 3, from which it can be seen that the relative error decreases with the cell size. The order of convergence is approximated using the error of the final position (ϵ)

$$\mathcal{O} = \frac{\ln(\epsilon_{\Delta x}/\epsilon_{\Delta x/2})}{\ln(2)} \quad (45)$$

Similar to the 1D Stefan problem, the distribution of \hat{s} to the pure gas cells results in a non-zero vapor velocity in a narrow region on the left of the interface and as the mesh is refined, the thickness of the non-zero velocity region reduces (Fig. 4(d)). More importantly, it is clearly shown that the liquid velocity on the right of the interface converges to the exact solution.

4.3. Spherical bubble growth in superheated liquid

In this test, we simulate the growth of a spherical vapor bubble surrounded by the superheated liquid [27,35,36,39,40]. The vapor is

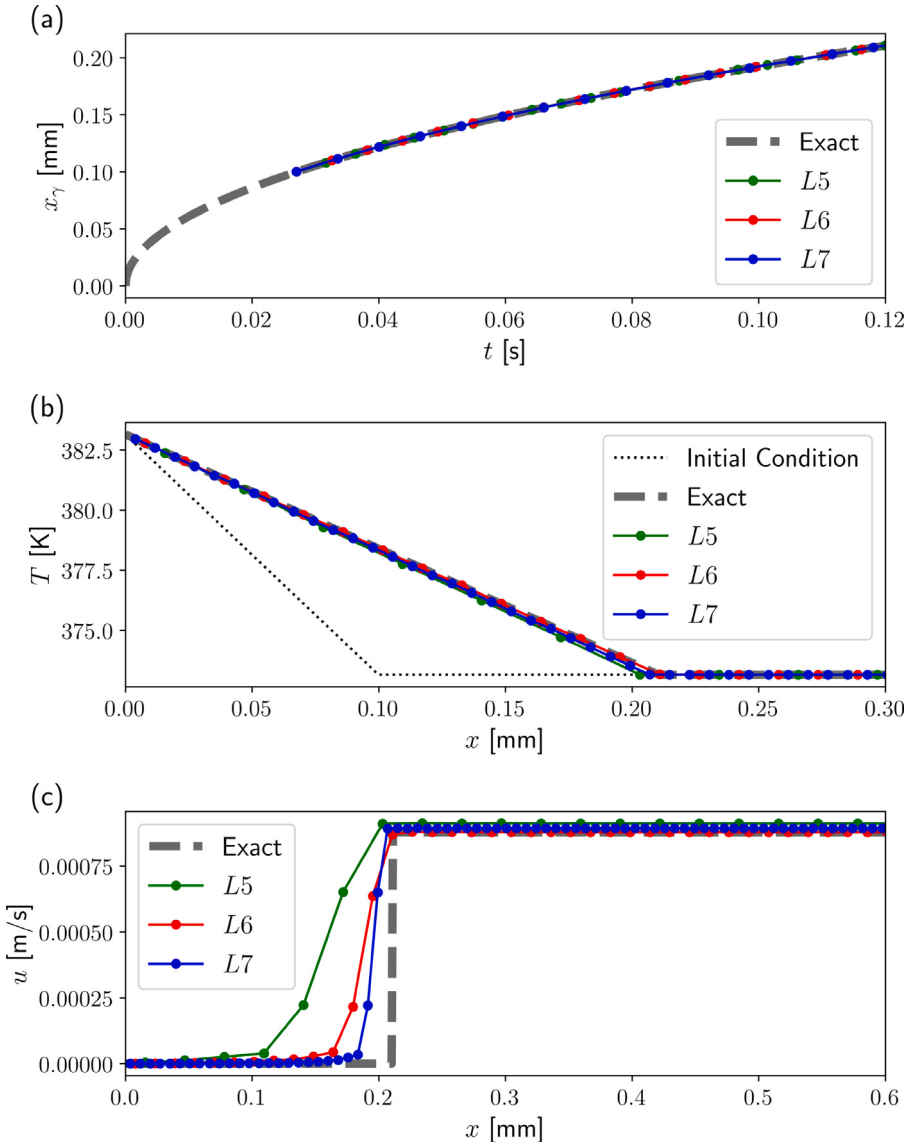


Fig. 3. Numerical results for the 1D Stefan problem for three levels of grid refinement: L_5 , L_6 , and L_7 , compared with the exact solution. (a) Temporal evolution of the interface position x_γ . (b) The overall temperature T ($T = T_g$ in vapor, $T = T_l$ in liquid, and $T = T_{sat}$ at the interface) and (c) the u -velocity distributions at the final time $t = 0.12$ s.

at saturation temperature T_{sat} and the liquid temperature in the far-field is fixed at $T_\infty > T_{sat}$. The heat flux from the liquid side drives vaporization and bubble growth. The gravity effect is ignored, so the bubble remains spherical as it grows. This problem is the spherically symmetric analog of the 1D sucking problem. The analytical solution for the temporal evolution of the bubble radius (R) is

$$R(t) = 2\beta\sqrt{\alpha_l t}, \quad (46)$$

where β is obtained by solving the following equation,

$$\begin{aligned} 2\beta^2 \int_0^1 \exp \left(-\beta^2 \left((1-\zeta)^{-2} - 2(1 - \frac{\rho_g}{\rho_l})\zeta - 1 \right) \right) d\zeta \\ = \frac{\rho_l C_{p,l}(T_\infty - T_{sat})}{\rho_g(h_{lg} + (C_{p,l} - C_{p,g})(T_\infty - T_{sat}))}. \end{aligned} \quad (47)$$

The liquid temperature is expressed as a function of r and t as

$$\begin{aligned} T_l(r, t) = T_\infty - 2\beta^2 \left(\frac{\rho_g(h_{lg} + (C_{p,l} - C_{p,g})(T_\infty - T_{sat}))}{\rho_l C_{p,l}} \right) \\ \int_{1-R(t)/r}^1 \exp \left(-\beta^2 \left((1-\zeta)^{-2} - 2(1 - \frac{\rho_g}{\rho_l})\zeta - 1 \right) \right) d\zeta. \end{aligned} \quad (48)$$

Fig. 5 shows the initial bubble ($R_0 = 1.2$ m) in the cubic computational domain with edge length $L_0 = 5R_0$. The octree mesh is plotted on the $x-y$ plane, and it can be seen that the mesh is refined to the maximum level near the interface to guarantee the interface and temperature gradient will be well captured. The fluid properties (Fluid A) are provided in Table 2 [36]. The exact solution for $t = 0.5$ s is used as the initial condition, and the simulation is run to $t = 0.21$ s.

The temperature distribution on the central $x-y$ cross-section is shown in Fig. 6(a). It can be seen that the bubble surface is spherical and smooth, as it is supposed to be. The temperature is fixed at T_{sat} inside the bubble and increases radially outward in the liquid from the interface location. A close-up of the interface is shown in Fig. 6(b), where the velocity field (vectors) and the magnitude of the temperature gradient (color) are plotted. The velocity jump across the interface can be clearly seen. More importantly, the velocity field obtained by the present method does not show artificial fluctuations of velocity magnitude or direction inside the bubble and at the interface, as observed in the previous studies (see Figs. 9–10 in Ref. [39] and Fig. 8 in Ref. [36]). The rate of vaporization (j_γ), computed based on the temperature gradient, is plotted in Fig. 6(c), which is non-zero only in the interfacial cells. The volumetric source s_γ is computed from j_γ

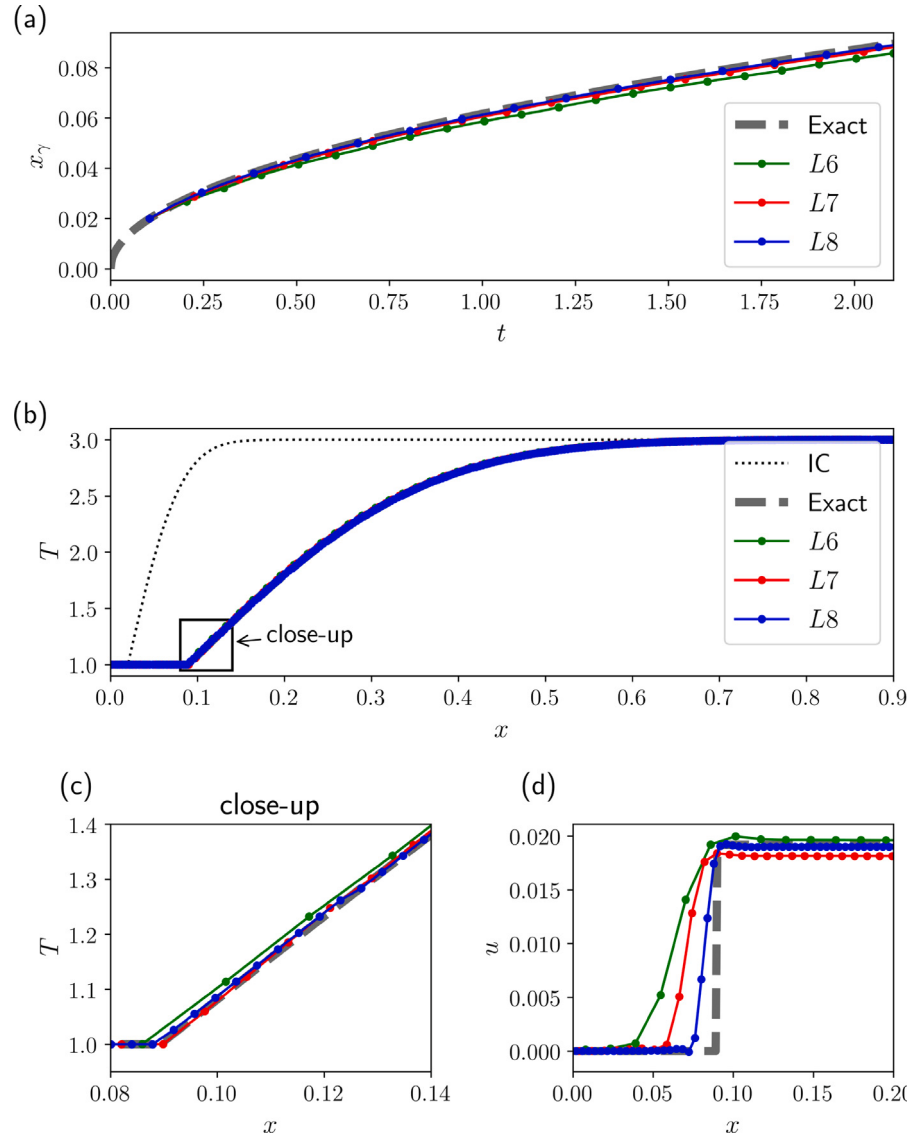


Fig. 4. Numerical results for the 1D Stefan problem for three levels of grid refinement: $L6$, $L7$, and $L8$, compared with the exact solution. (a) Temporal evolution of the interface position x_γ . (b)-(c) The overall temperature T and (d) the u -velocity distributions at the final time $t = 2.1$ s. Note that (c) is a close-up of the temperature distribution near the interface - see annotation in (b).

using Eq. (6) and is then distributed to the neighboring pure gas cells, and the distributed source \hat{s} is plotted in Fig. 6(d). It can be seen that \hat{s} is smoothly distributed in the nearby pure gas cells and the gas cells close to the interface receive a bigger share.

The temporal evolution of the bubble radius and the radial distribution of temperature at the final time are presented in Fig. 7. It is observed that both the numerical results converge toward the analytical solution when the mesh is refined from $L7$ to $L9$. The results for $L9$ agree with the exact solution very well. The values of the bubble radius and the relative errors at the final time for various levels of refinement are provided in Table 4. It is clear that the error is reduced when the mesh is refined.

4.4. Film boiling

The last validation test case to be presented is the 2D film boiling problem, see Fig. 8 [25,71–75]. The buoyancy effect is included which triggers the Rayleigh–Taylor instability (RTI) at the interface. Compared to the previous tests, which involve only 1D flows, this test exhibits 2D flows and more complex interface deformation.

Table 4

The relative error of the interface position at the final time for the spherical bubble problem and the order of convergence \mathcal{O} .

| Maximum grid level | Final radius | Relative error (%) | \mathcal{O} |
|--------------------|--------------|--------------------|---------------|
| $L7$ | 0.231 | 3.7 | – |
| $L8$ | 0.236 | 1.44 | 1.36 |
| $L9$ | 0.239 | 0.26 | 2.47 |

The most unstable wavelength for inviscid RTI with surface tension is given as

$$\lambda_d = 2\pi \sqrt{\frac{3\sigma}{(\rho_l - \rho_g)g}}, \quad (49)$$

based on this we have set the computational domain $x = [-\lambda_d/2, \lambda_d/2]$ and $y = [0, \lambda_d]$, so that the width of the domain covers one most-unstable wavelength. The initial interface is perturbed with a single mode and the interfacial position is expressed as

$$y = \frac{\lambda_d}{128} \left[4 + \cos \left(\frac{2\pi x}{\lambda_d} \right) \right]. \quad (50)$$

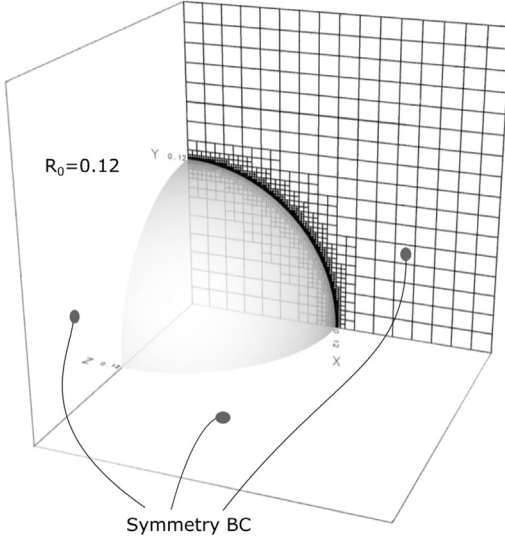


Fig. 5. The 3D computational domain for a spherical bubble in a superheated liquid.

The fluid properties are provided in Table 2 (Fluid B) and the gravitational acceleration is $g = 9.81 \text{ m/s}^2$. The bottom wall is a no-slip boundary at a constant elevated temperature $T_{wall} = T_{sat} + 5 \text{ K}$. The left and right boundaries are symmetry boundary conditions and the top boundary is an outlet boundary condition. Initially, the fluids are stationary and the temperature is varied linearly in the vapor between the wall and the interface (see Fig. 8).

Fig. 9(a) shows the temporal development of the interface from $t = 0.24$ to 0.528 s at a constant increment of 0.036 s . The development of the RTI bubble can be clearly seen. In Fig. 9(c), the present results at $t \approx 0.24 \text{ s}$ for different mesh refinement levels are compared to the numerical results of Sun et al. [73]. Again, the present numerical

results converge as the mesh is refined, and the results for $L11$ are in good agreement with the previous numerical results using a uniform mesh. The solution appears to have converged at $L10$ as the difference between results for $L10$ and $L11$ is almost invisible (Fig. 9(c)). Additionally, the increase of vapor volume over time is shown in Fig. 9(d). Here, the vapor volume in the domain Ω , i.e., $V_g = \int_{\Omega} (1 - c) dV$, is normalized by its initial value $V_{g,0}$. In Fig. 9(d), the difference in volume from $L10$ to $L11$ is negligible.

The temporal evolution of the space-average Nusselt number Nu is shown in Fig. 9, where $\text{Nu} = \int \text{Nu}^* dx / \lambda_d$ and the local Nusselt number is defined as

$$\text{Nu}^* = \frac{\lambda'}{T_{wall} - T_{sat}} \left. \frac{\partial T}{\partial y} \right|_{y=0} \quad \text{where } \lambda' = \sqrt{\frac{\sigma}{(\rho_l - \rho_g)g}}. \quad (51)$$

The simulation result of Nu is compared to the Klimenko correlation [72] which predicts Nu to be 1.91 [76]. Initially, Nu decreases as the interface moves away from the wall. Then, as the RT instability develops, Nu increases as the RT bubble grows. The temporal evolution of Nu matches perfectly with the results of Guo et al. [76] up until about $t = 0.2 \text{ s}$, after which we observe an earlier increase in Nu . This discrepancy is probably due to the higher mesh resolution and the more accurate VOF method used in the present simulation. The adaptive mesh of $L11$ used in the present simulation is equivalent to 2048 cells across λ_d , compared to the mesh of Guo et al. [76] where there are only 64 cells. The high mesh resolution has also avoided the early numerical breakup of the stem connecting the bubble and the film observed in previous simulations [22,73,76].

5. Deformation and breakup of a vaporizing drop

The results for the above validation cases and the good agreement with exact solutions and previous numerical studies have affirmed that the present methods and the implementation in the *Basilisk* code are capable of accurately resolving interfacial liquid–gas two-phase flows with vaporization. In this section, the code will be applied to simulate

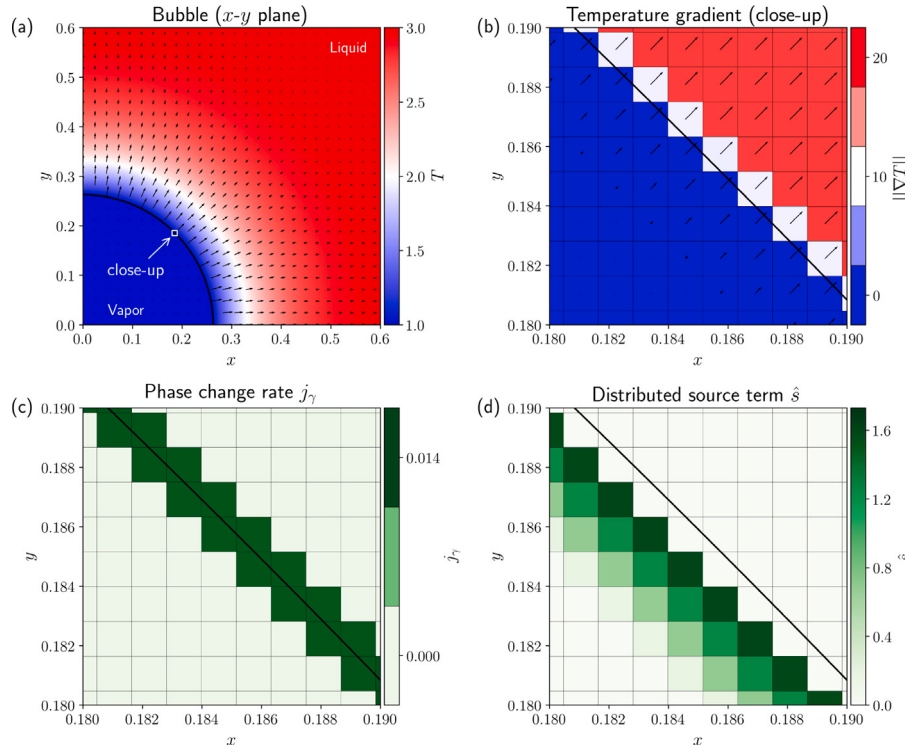


Fig. 6. Bubble x - y plane cross-section at $t = 0.21$ showing (a) the temperature distribution and the velocity quiver plot. Three close-up depictions of cells near the interface showing (b) the magnitude in the temperature gradient, (c) the rate of phase change at the interface (j_{γ}), and (d) the distributed phase-change source term (\hat{s}).

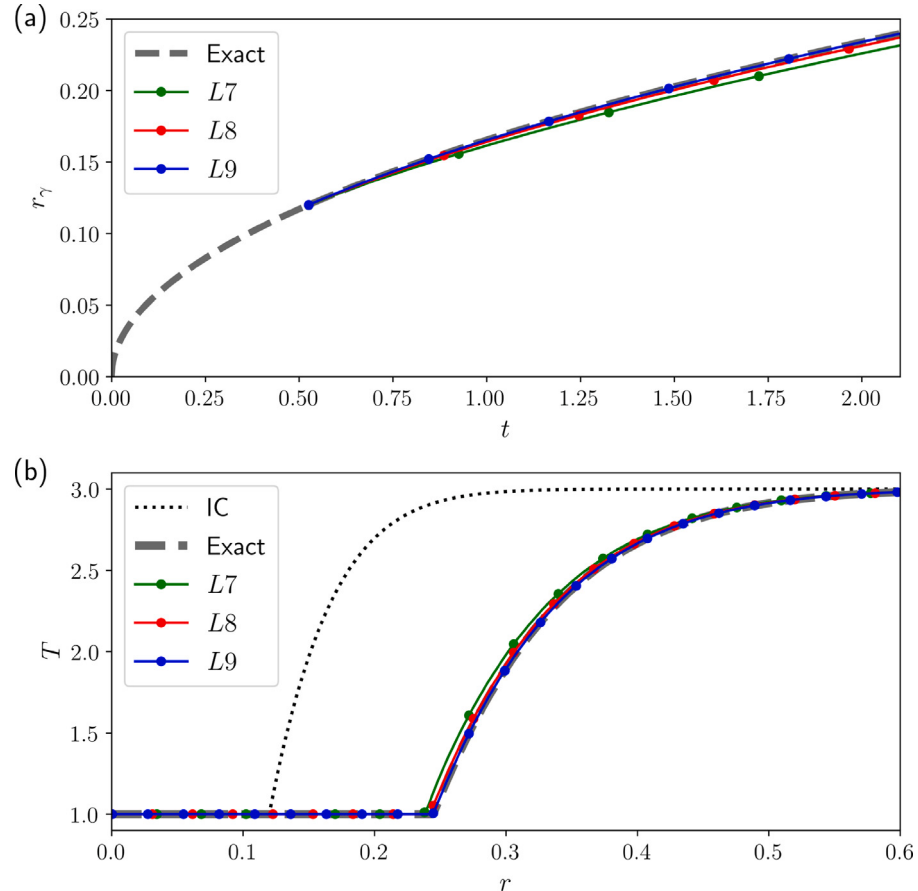


Fig. 7. Numerical results for the spherical bubble growth problem for three levels of grid refinement: $L7$, $L8$, and $L9$, compared with the exact solution. (a) Temporal evolution of the radial interface position r_γ . (b) Temperature distribution at the final time $t = 0.21$ s.

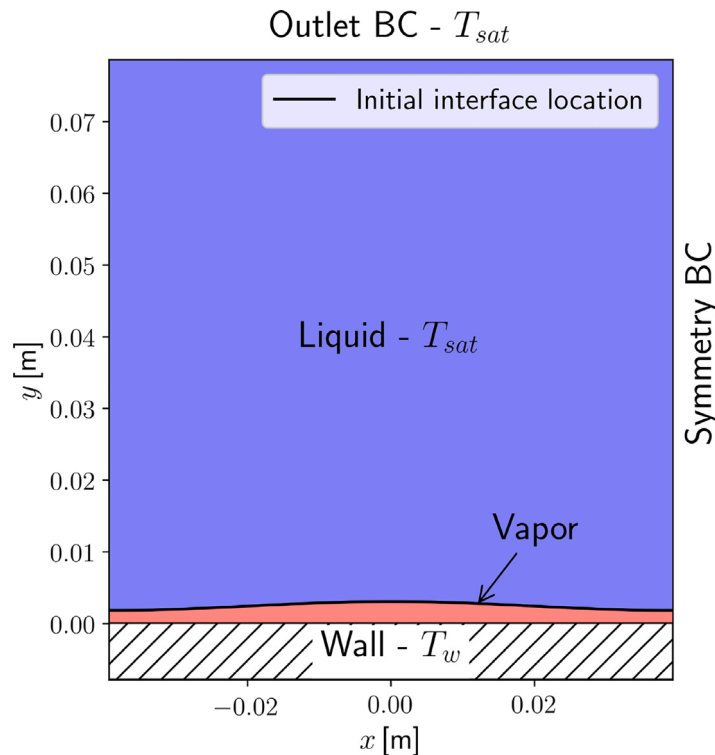


Fig. 8. The schematic of the computational domain for the film boiling problem.

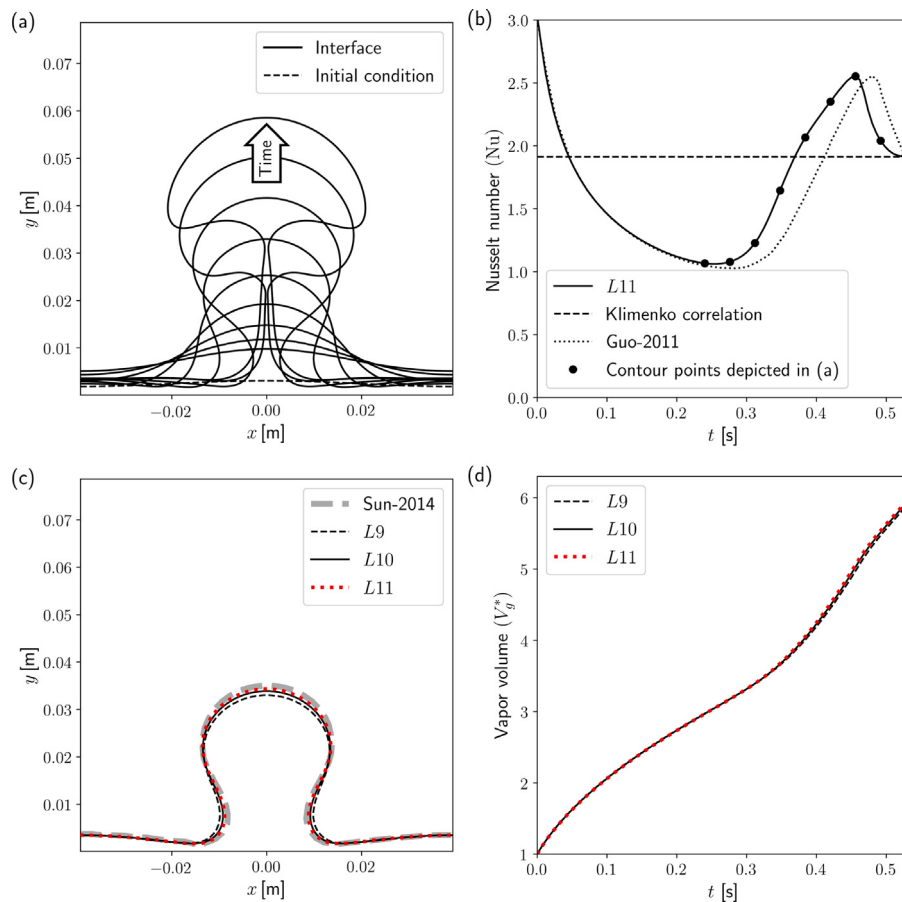


Fig. 9. (a) The temporal evolution of the interface from $t = 0.24$ s to $t = 0.528$ s at increments of 0.036 s at L11, (b) the Nusselt number evolution in time compared to the Klimentko correlation [72,76], and (c) the interface shape of the film boiling problem at three levels of refinement (L9, L10, and L11) compared to the results from Sun et al. [73] at $t \approx 0.24$ s. (d) The evolution of the normalized vapor volume in the domain, $V_g^* = V_g/V_{g,0}$.

the aerodynamic breakup of a vaporizing drop in a uniform hot gas stream.

It is considered here that a spherical drop at saturated temperature ($T = T_{\text{sat}}$) is stationary at $t = 0$ and is suddenly exposed to an unbounded uniform hot vapor stream ($T = T_{\infty}$) at $t = 0^+$. When vaporization is absent ($T_{\infty} = T_{\text{sat}}$), the drop dynamics and topology evolution are fully determined by the densities and viscosities of the drop liquid and the gas, ρ_l , μ_l , ρ_g , μ_g , the surface tension σ , the initial drop diameter D_0 , and the uniform gas stream velocity U_{∞} . The subscript 0 is used to represent the initial state. These parameters lead to four independent dimensionless parameters: the Weber number, $\text{We} = \rho_g U_{\infty}^2 D_0 / \sigma$, the Reynolds number, $\text{Re} = \rho_g U_{\infty} D_0 / \mu_g$, the Ohnesorge number, $\text{Oh} = \mu_l / \sqrt{\rho_l D_0 \sigma}$, and the gas-to-liquid density ratio, $\eta = \rho_g / \rho_l$ [77–80]. Alternative dimensionless parameters can be defined based on the above four parameters [80]. For drops with low Oh, such as millimeter drops of low-viscosity liquids like water, the viscous stress is small compared to surface tension and thus the latter is the dominant stabilization mechanism against drop deformation and breakup. In such cases, We is the most important parameter and is typically used to characterize the breakup modes. For low-Oh drops, the critical Weber is number $\text{We}_{cr} = 11 \pm 2$ [80,81], and the drop will break only when $\text{We} > \text{We}_{cr}$. Recent detailed numerical simulations of drop aerobreakup indicated that 2D axisymmetric simulations yield good approximation only for non-breaking drops at low We and Re [82]. For drops with high We and Re, which will break in a bag or multi-bag mode, fully 3D simulations are required to accurately capture the drop dynamics. Here we consider two cases of different We. In the first case, we considered a water drop at $\text{We} = 1.5$ and $20 < \text{Re} < 200$. Since We is significantly lower than We_{cr} , the drop will not break and the deformation is mild,

so 2D axisymmetric simulations were performed. In the second case, we have considered an acetone drop at $\text{We} = 62.7$. The drop will break and thus a fully 3D simulation was conducted.

When $T_{\infty} > T_{\text{sat}}$, vaporization will occur and the rate is controlled by the Stefan number (also referred to as the Spalding and Jakob numbers), $\text{St} = C_{\rho,g}(T_{\infty} - T_{\text{sat}})/h_{lg}$. In both cases considered here, St is about 0.1. When the drop deformation is not negligible, the increase in the interfacial area will result in an increase in the drop vaporization rate. In such cases, the heat and mass transfer between the drop and the surrounding vapor will deviate from the models for spherical drops [54], which is strictly valid for zero We.

Sub-grid drop vaporization models for drops are important to the accurate simulation of sprays in practical applications. For sprays consisting of a large number of drops, it is inivable to resolve the interface for each individual drop. Instead, a drop is modeled as a point mass (or a group of drops as a parcel), which is known as the Lagrangian point-particle (LPP) approach [83]. Since the flow and temperature fields in the drop scale are not resolved, physical models are required to account for the momentum, heat, and mass transfer between the drop and the surrounding gas and to predict the children droplets generated after breakup [84–86]. For drops with finite We, the drop deformation/breakup and vaporization are closely coupled. LPP models that can accurately capture this coupling effect remain to be established. High-fidelity detailed numerical simulations, enabled by the present method, can provide crucial insights into the currently unclear physics and, thus, are important to the development of such models in the future.

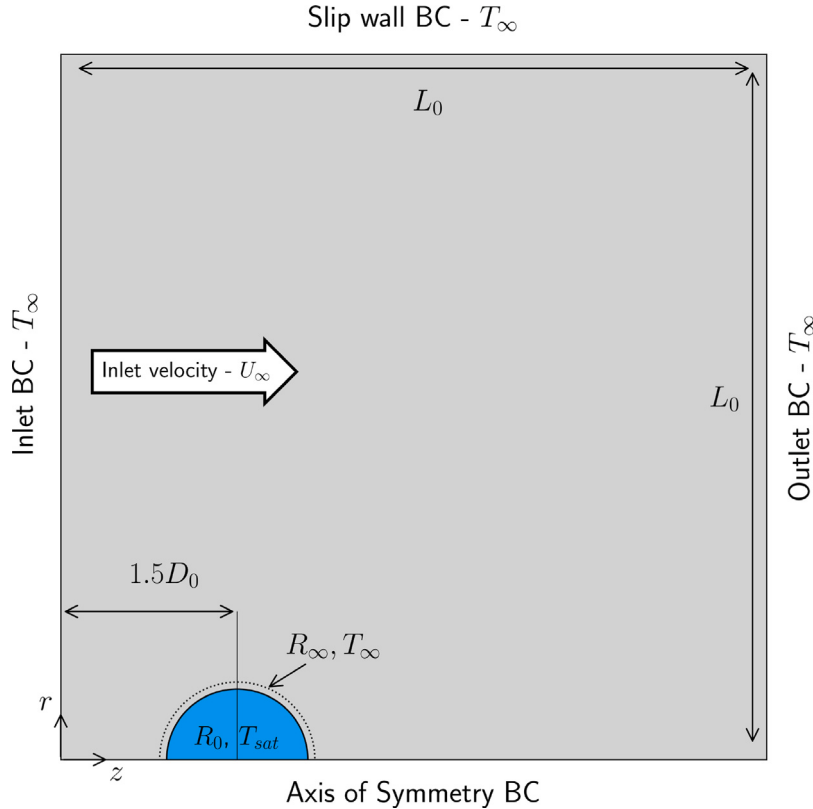


Fig. 10. The computational domain for 2D-axisymmetric simulation of the vaporization of a freely moving drop in a hot vapor stream.

5.1. Axisymmetric 2D simulations for a vaporizing drop at low We

We first consider a water drop at a low Weber number. The water properties are provided in Table 2 where the Prandtl number of water in steam is $\text{Pr} \approx 1$. The drop is initially spherical with a radius R_0 . A parametric study has been performed by varying the Reynolds number, *i.e.*, $22 < \text{Re} < 200$, and there are in total 25 cases simulated. For each case, we have modified the free stream velocity U_∞ and surface tension (σ) simultaneously to keep the Weber number fixed at $\text{We} = 1.5$. Due to the low We and Re, the drop deformation is mild. Therefore, 2D axisymmetric simulations are sufficient to capture the drop dynamics and vaporization. For all cases, the free-stream temperature is set to $T_\infty \approx 600\text{ K}$, which yields $\text{St} = 0.1$.

The computational domain for the 2D axisymmetric simulation is shown in Fig. 10. The domain is a square with the edge length $L_0 = 8D_0$. The drop is initially located at $x = 1.5D_0$. For all cases, we have run the simulations with $L12$ (equivalent to $\Delta x = D_0/512$) to $t^* = 0.16$, unless stated otherwise. Note that t^* is the dimensionless time defined as [87]

$$t^* = t \frac{U_\infty}{D_0 \sqrt{\rho_l / \rho_g}}. \quad (52)$$

Within this short time duration, the drop velocity change is very small due to the large density contrast between the liquid and vapor. As a result, the relative velocity can be approximated as unchanged, so Re and We remain to be their initial values. After a short time duration for the velocity and thermal boundary layer to develop from the initial condition, the drop vaporization rate reaches an approximate quasi-steady state, until then we will measure its value. To shorten the transition to the quasi-steady state, the initial condition for the temperature is specified as

$$T(r) = \begin{cases} T_{\text{sat}}, & \text{if } r \leq R_0 \\ T_\infty, & \text{if } r \geq R_\infty \\ \frac{R-R_0}{R_\infty}(T_\infty - T_{\text{sat}}) + T_{\text{sat}}, & \text{otherwise} \end{cases} \quad (53)$$

where we set $R_\infty = 1.25R_0$ as shown in Fig. 10. As long as the artificial thermal boundary layer thickness is small, $R_\infty - R_0 \ll R_0$, the specific value of R_∞ is immaterial and will not influence the reported results. For all the cases simulated, a quasi-steady state was reached before $t^* = 0.06$.

Extensive experimental studies have been conducted for the vaporization of a spherical drop at a quasi-steady state, from which the empirical relations for the Nusselt (Nu) number have been extracted [17,54,88–90]. A commonly used empirical model is the one developed by Renksizbulut and Yuen [54], which can be expressed as

$$Z_f \equiv [\text{Nu}(1 + \text{St})^{0.7} - 2]\text{Pr}_f^{-1/3} = 0.57\text{Re}_f^{1/2} \quad (54)$$

where $\text{Re}_f = 2R\rho_{g,\infty}|\mathbf{u}_\infty - \mathbf{u}_d|/\mu_f$ and $\text{Pr}_f = C_{p,f}\mu_{g,f}/k_f$ are the Reynolds and Prandtl numbers based on the film properties. The subscript f indicates that the parameters for the gas film surrounding the drop ($T_f = (T_\infty + T_{\text{sat}})/2$). The variation in gas properties due to temperature variation in the film is ignored, so $\text{Re}_f = \text{Re}_\infty$. The drop vaporization experiments were conducted for a range of Reynolds, Stefan, and Prandtl numbers: $25 < \text{Re} < 2000$, $0.07 < \text{St} < 2.79$, and $0.7 < \text{Pr} < 1$ [54]. Eq. (54) is therefore valid within these parameter ranges. Furthermore, it is considered the drop temperature is initially at T_{sat} , and heat transfer by radiation is neglected. Based on the convective heat transfer characterized by Nu, the rate of change of drop volume can then be computed as

$$\dot{V}_l = \frac{-\dot{q}A_s}{\rho_l h_{fg}}, \quad (55)$$

where the drop surface area is $A_s = 4\pi R_0^2$, the convective heat transfer coefficient is $h = \text{Nu}k_g/(2R_0)$, and the rate of heat transfer is $\dot{q} = h(T_\infty - T_{\text{sat}})$.

Fig. 11 shows the temperature and velocity fields at the end of the simulation ($t^* = 0.16$) for $\text{Re} = 200$. As expected, the temperature gradient is higher on the windward surface of the drop (Fig. 11), as a result, the majority of the vaporization occurs near the front stagnation

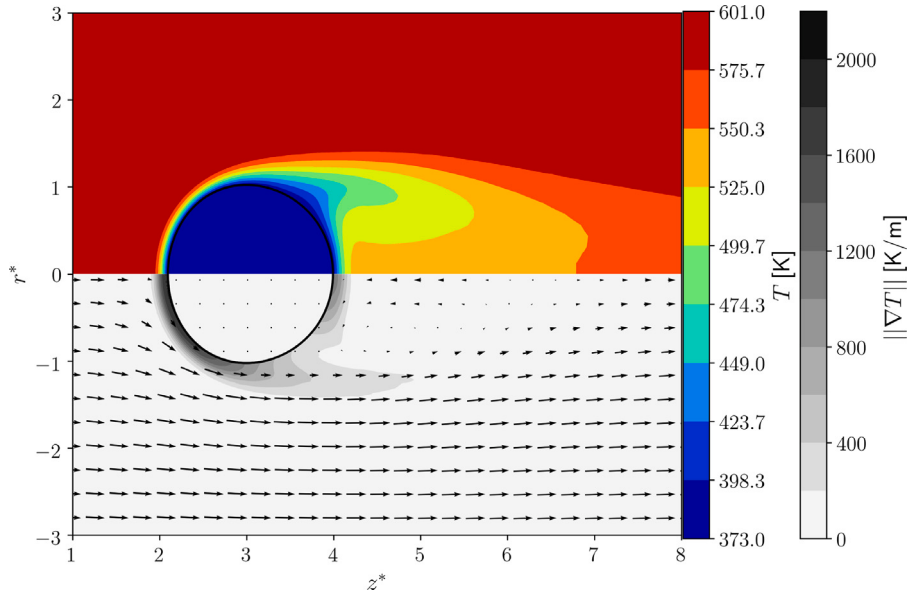


Fig. 11. Temperature (top), the temperature gradient magnitude, and velocity field (bottom) for a moving water drop in high-temperature vapor steam at $t^* = 0.16$ for $We = 1.5$ and $Re = 200$. The black contour line represents the drop surface. For better visualization, the velocity vectors are only plotted in the mesh refinement level 6. Note that $r^* = r/R_0$ and $z^* = z/R_0$.

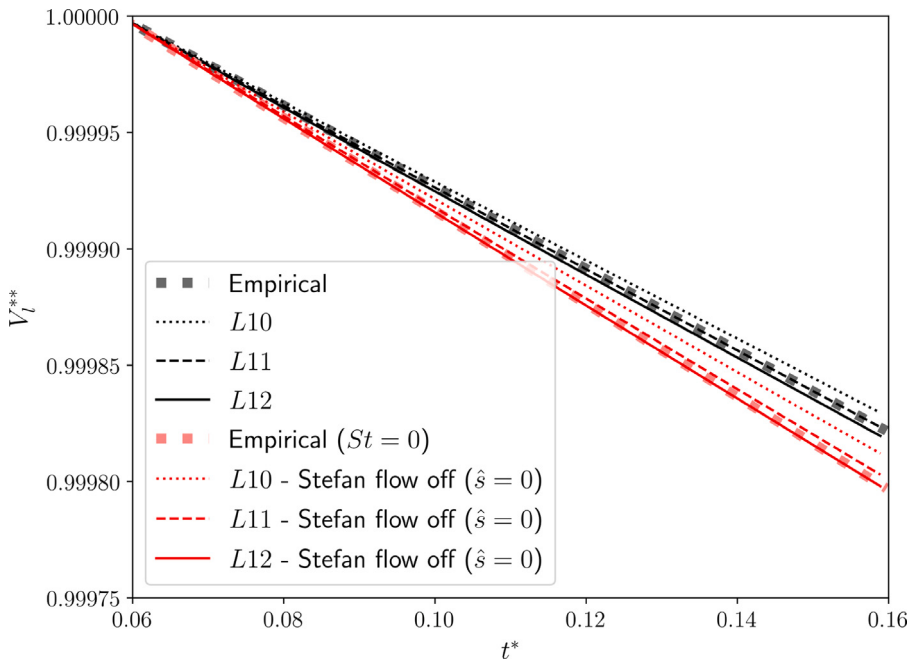


Fig. 12. Simulation results for the decrease of drop volume due to vaporization, with and without the Stefan flow, for $Re=126$. The corresponding empirical correlations are also shown for comparison. To visualize the rate of liquid volume loss, the droplet volume is non-dimensionalized using $V_l^{**} = V_l/V_l(t^* = 0.06)$, where the quasi-steady state is achieved before $t^* = 0.06$.

point [91]. On the leeward side of the drop, the temperature gradient is much lower since the gas temperature is low in the wake, where the gas is cooled by the low-temperature drop.

The simulation results for the temporal evolution of the drop volume are shown in Fig. 12, compared with the empirical model (Eq. (55)). The simulation results *without* the Stefan flow are also shown to demonstrate the effect of the Stefan flow on the rate of vaporization. The Stefan flow is turned off by manually setting $\hat{s} = 0$ in Eq. (36). Note we still consider the vaporization when we turn off the Stefan flow; *i.e.*, $\hat{s} = 0$ and $s_\gamma \neq 0$, resulting in a reduction in the droplet volume (Fig. 12). The empirical model without the Stefan flow will simplify Eq. (54) by setting $St = 0$ [17]. For both cases, with and without Stefan flow,

the simulation results converge as the refinement level increases from $L10$ to $L12$. The simulation results for $L12$ and the empirical models agree very well. The Nusselt number measured from the simulations is compared with the predictions of the empirical model in Table 5 and an excellent agreement is observed. The Stefan flow of lower-temperature vapor (at T_{sat}) will reduce the temperature gradient at the interface and thus will result in a decrease in the rate of heat and mass transfer. Therefore, ignoring the Stefan flow will lead to an overestimation of the rate of drop vaporization, therefore, it is important to accurately capture the Stefan flow in a simulation.

Finally, the simulation results for different Re (with mesh $L11$) are shown in Fig. 13, compared with the empirical correlation (Eq. (54)).

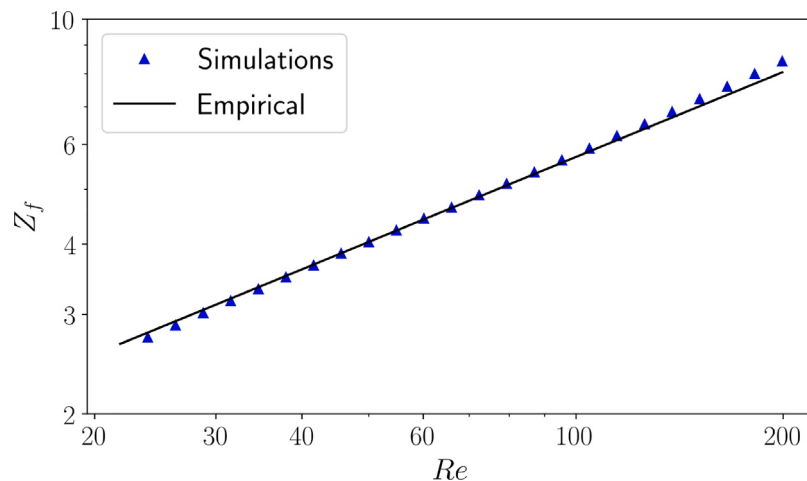


Fig. 13. Simulation results for different Re between 20 and 200, compared with the empirical correlation (Z_f is defined in Eq. (54)).

Table 5

The Nusselt numbers with and without Stefan flow for various levels of grid refinement (L_{10} , L_{11} , L_{12}) compared to the empirically predicted Nu.

| Case | Nu | Nu (without Stefan flow) |
|-----------|------|--------------------------|
| L_{10} | 7.12 | 7.84 |
| L_{11} | 7.38 | 8.22 |
| L_{12} | 7.53 | 8.43 |
| Empirical | 7.42 | 8.44 |

The parameter Z_f in Eq. (54) scales with $Re^{1/2}$, and the simulation results agree well with this scaling relation. The computed values of Z_f match quite well with the empirical model for the whole range of Re considered. The small discrepancy may be due to the small drop deformation in the simulations since we did not constrain the drop to be perfectly spherical as in the experiment. The good agreement observed here further validates the present methods in simulating the vaporization of a slightly deforming drop.

5.2. Fully 3D simulation for the breakup of a vaporizing drop

The value of We has been increased in the second case, as a result, the vaporizing drop deforms significantly and eventually breaks. The drop fluid is acetone and the initial diameter is $4.1 \mu\text{m}$. The free-stream gas is acetone vapor. The liquid and vapor properties are provided in Table 6. The free-stream gas velocity, pressure, and temperature are $U_\infty = 214.4 \text{ m/s}$, $p_\infty = 285 \text{ kPa}$, and $T_\infty = 402 \text{ K}$, respectively. These parameters are chosen to be similar to the post-shock conditions for a planar shock wave with Mach number 1.6, inspired by the shock tube experiment of Duke-Walker et al. [48], though the present simulation has neglected the effects of shock-drop interaction and compressibility. A 3D simulation is performed in this case and Fig. 14 shows the cubic computational domain, the edge size of which is $L_0 = 16D_0$. The origin is at the center of the left surface of the domain. The initial position of the drop is $(x, y, z) = (1.5D_0, 0, 0)$. The simulation has been run to $t^* = 2$.

To simplify the analysis, the drop is assumed to be initially at T_{sat} and the variation in the gas properties due to temperature is ignored. The key non-dimensional parameters are $\text{We} = 62.7$, $\text{Re} = 468$, $\text{Oh} = 0.0277$, $\eta = 0.0072$, $\text{Pr} = 0.844$, and $\text{St} = 0.127$. The time step is determined based on $\text{CFL} = 0.5$. The maximum level of refinement is $L = 12$, resulting in a minimum cell dimension $\Delta x = D_0/256$. The total number of octree cells is approximately 11 million (equivalent to 69 billion uniform Cartesian cells). The simulation has been run on the Anvil machine for 3 days using 256 cores (AMD Epyc Milan processor).

The deformation and breakup of the vaporizing acetone drop are shown in Fig. 15. The time snapshots are from $t^* = 0$ to 2.0 with an

Table 6

Acetone fluid properties.

| Property | Acetone | |
|--|-----------------------|-----------------------|
| | Liquid | Vapor |
| $\rho [\text{kg/m}^3]$ | 710 | 5.11 |
| $k [\text{W m}^{-1} \text{K}^{-1}]$ | 0.156 | 0.0166 |
| $C_{p,g} [\text{J kg}^{-1} \text{K}^{-1}]$ | 2420 | 1460 |
| $\mu [\text{Pa s}]$ | 1.85×10^{-4} | 9.59×10^{-6} |
| $h_{fg} [\text{J kg}^{-1}]$ | 4.88×10^5 | - |
| $T_{\text{sat}} [\text{K}]$ | 359 | - |
| $\sigma [\text{N m}^{-1}]$ | 0.0153 | - |

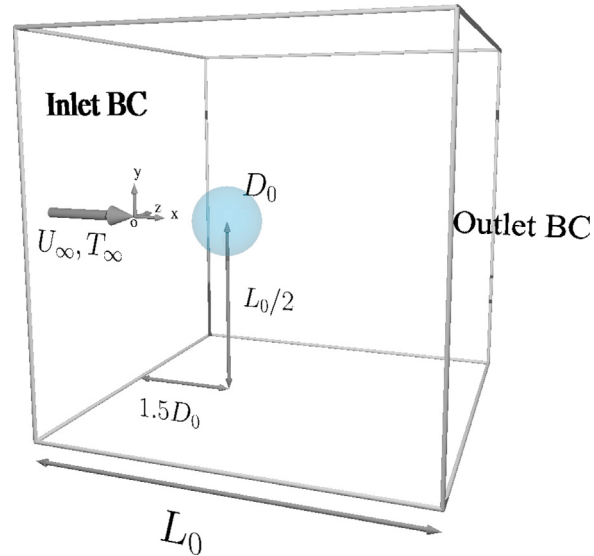


Fig. 14. Schematic of the 3D computational domain for 3D acetone drop exposed to a uniform high-temperature vapor stream.

increment of 0.1. To better illustrate the interaction between the drop and the surrounding vapor, Fig. 16 shows the drop surface along with the contours of the temperature (T) and velocity magnitude ($\|\mathbf{u}\|$) from the central $x-z$ and $x-y$ planes.

In a very short time after the initially stationary drop is exposed to the gas stream, the viscous and capillary effects are negligible and the flow field is dominated by the inviscid mechanisms. The two stagnation points can be seen on both the windward and leeward poles of the drop.

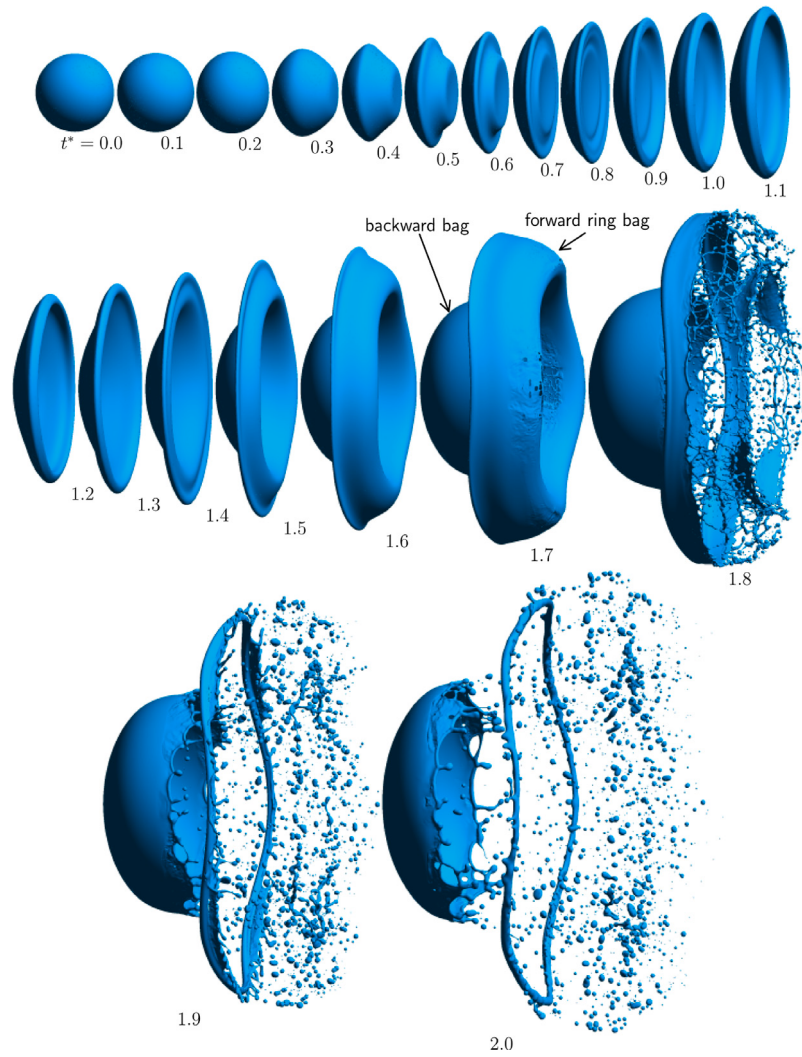


Fig. 15. Morphological evolution of the vaporizing drop from $t^* = 0$ to 2 at time increments of $\Delta t^* = 0.1$.

As a result, the drop is compressed in the streamwise direction, and the shape of the drop is approximately symmetric with respect to the central y - z plane normal to the streamwise direction, see $t^* = 0$ to 0.2. As time evolves, the boundary layer separates and the wake starts to form. The leeward side of the drop becomes flat ($t^* = 0.3$ to 0.5). The streamwise compression of the drop results in lateral expansion and an “edge” of high curvature is formed at the periphery. The high gas velocity at the periphery results in a strong shear, and the shear Kelvin-Helmholtz (KH) like instability drives the edge roll over the back of the drop, turning the drop to a bowl with the opening facing downstream (sometimes also referred to as a backward bag) ($t^* = 0.6$ to 1.3). As the drop continues to expand in the lateral direction, Rayleigh-Taylor (RT) instability develops on the windward surface near the periphery, turning the drop from a bowl to a shape similar to a Sombrero hat ($t^* = 1.4$ to 1.7). The drop at $t^* = 1.7$ consists of both a backward bag near the central axis and a forward ring bag. This complex shape is the outcome of both the KH and RT instabilities and this drop morphology has been observed for moderate We when η is not too small [46,92]. The high-speed gas blows in the forward ring bag and causes it to inflate rapidly, resulting in a fast decrease in the sheet thickness. At around $t^* = 1.8$, holes appear in the forward ring bag. The expansion and merging of multiple holes disintegrate the ring bag, forming a large number of small children drops, an unbroken backward bag, and a circular rim ($t^* = 1.8$ to 2.0). To simulate the subsequent breakup of the remaining backward bag and rim, a longer simulation in a

larger domain is required. Yet such a simulation is out of the scope of this paper since the purpose of the present test is to demonstrate the capability of the present methods.

The vaporization here is driven by the superheated free stream, and the rate of vaporization depends on the vapor temperature gradient near the interface. It can be observed from Fig. 16 that the temperature gradient magnitude is higher on the windward side of the drop, where stronger vaporization occurs. The vapor generated is at a lower temperature (T_{sat}) compared to the free-stream temperature (T_{∞}). The low-temperature vapor is entrained in the wake and mixed with the free-stream hot vapor. As a result, the temperature gradient on the leeward side of the drop is lower and less vapor is produced, see Fig. 16(c)-(d).

As the drop deforms, the drop surface area increases. Corresponding to that, the drop vaporization rate (the rate of loss of drop volume) also increases. The time evolution of the drop volume is shown in Fig. 17(a). The empirical relation for a non-deformable spherical drop (Eq. (54)) is also plotted for comparison. When the drop is perfectly spherical, the volume decreases at a constant rate. For $t^* = 0$ to 0.4, the drop remains approximately spherical, see Fig. 15. As a result, the drop volume decreases linearly in time, and the simulation results agree well with the empirical correlation, similar to the low-We drop considered previously in Section 5.1. As time evolves and the drop deformation becomes more significant, the vaporization rate goes up and the drop volume decreases significantly faster, due to the increase of drop surface area, in particular the area of the windward/frontal surface. To

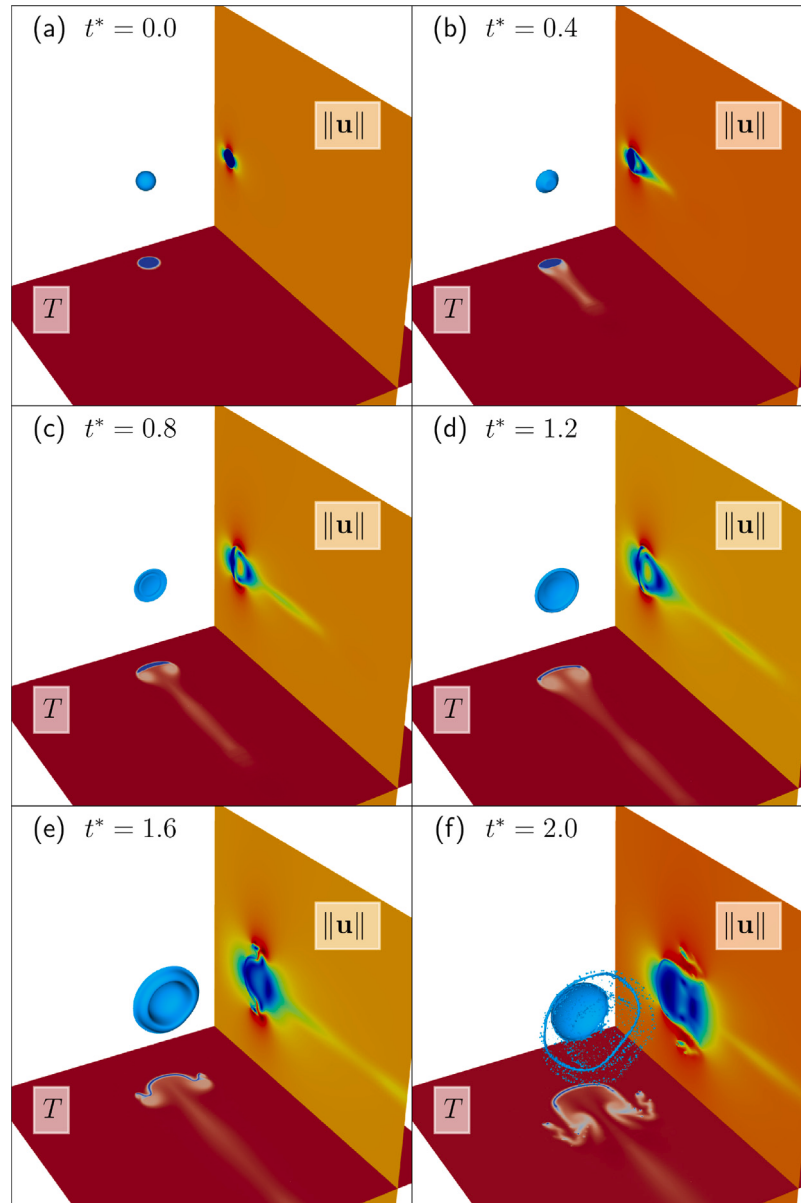


Fig. 16. Snapshots of the drop surface, the temperature (T) on the central x - y plane, and the velocity magnitude ($\|u\|$) on the central y - z plane from $t^* = 0$ to 2 at time increments of $\Delta t^* = 0.4$.

better illustrate the relationship between the drop vaporization rate and the frontal surface area, Fig. 17(b) shows the temporal evolution of the normalized vaporization rate $(dV_l/dt)^* = (dV_l/dt)/(dV_l/dt)_0$ and the normalized frontal or windward surface area of the drop, $A_f^* = A_f/A_{f,0}$. The results clearly show that the increase in frontal area is closely related to the increasing rate of volume loss.

The inflation of the forward ring bag starts at approximately $t^* = 1.6$, after which the increase in the frontal surface area seems to contribute less to the enhancement of vaporization, and $(dV_l/dt)^*$ reaches a plateau at about 15. This is probably due to the fact that the strong convective effect in the gas flow in the forward ring bag has reduced the temperature gradient magnitude near the interface, see Fig. 16(e). After the forward ring bag breaks, the rapid vaporization of the small drops generated dominates the loss of the total liquid volume over time. Yet it should be noted that even though a high mesh resolution has been used in the present simulation, some of the tiny children droplets generated are still not well resolved. The temperature gradient and vaporization rate for those small drops may be underestimated. Since the Weber number for these tiny drops is very small, they typically

exhibit a spherical shape with very mild deformation. Therefore, it will be more computationally efficient to model the vaporization of these tiny drops through the Lagrangian point-particle approach, instead of resolving them with the VOF method and a finer mesh, see for example the multiscale VOF-LPP model in the previous studies for drop dynamics [93–95]. Nevertheless, such a model that can incorporate heat transfer and vaporization remains to be established.

6. Conclusions

A consistent volume-of-fluid method has been developed in the present study for the direct numerical simulation of interfacial multiphase flows with phase change. The geometric VOF method is based on Piece-wise Linear Interface Calculation (PLIC) reconstruction and the advection of momentum and energy is consistent with the VOF advection. A novel method is proposed to distribute the volumetric source, induced by vaporization at the interfacial cells, to the neighboring pure gas cells. With this simple but elegant treatment, the velocity at the interfacial cells is not influenced by the Stefan vapor flow and can be used

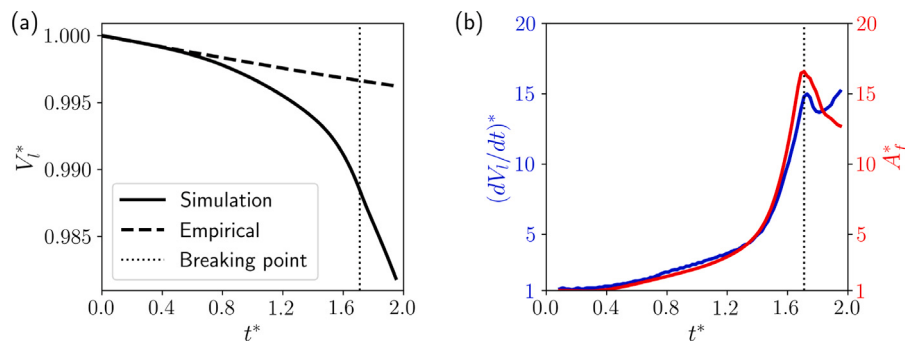


Fig. 17. Temporal evolution of (a) the drop volume ($V_l^* = V_l/V_{l,0}$) and (b) the rate of vaporization normalized by empirical vaporization rate ($[dV_l/dt]^*$) and the frontal surface area of the droplet ($A_f^* = A_f/A_{f,0}$). The empirical correlation (Eq. (54)) is also shown in (a) for comparison. The vertical dotted line indicates the onset of the breakup of the forward ring bag ($t^* \approx 1.7$).

to advect the interface directly. The additional shifting of the interface toward the liquid side due to vaporization is handled geometrically, using the interface normal obtained in interface reconstruction. The present method does not require an additional pressure equation and projection as needed in previous studies. Furthermore, the Stefan flows near the interface do not exhibit any artificial numerical oscillations, as observed in previous studies, due to the estimate of the vaporization rate.

The present methods have been implemented in the open-source solver *Basilisk* using the octree/quad-tree mesh. The developed simulation framework has been tested against various benchmark cases. For all cases considered, the simulation results converge as the mesh is refined. The simulation results agree very well with the exact solutions for the 1D Stefan and sucking problems and the growth of a 3D spherical bubble in superheated liquid. The code has also been used to simulate a 2D film boiling problem and the simulation results agree well with previous numerical results obtained using a uniform mesh.

To further test the capability of the present methods in resolving freely moving vaporizing drop, 2D axisymmetric simulations have been conducted to study the vaporization of a water drop in a high-temperature superheated vapor stream. The Weber number is 1.5 and thus the drop deformation is mild. A parametric study is carried out by varying the Reynolds number (Re) from 20 to 200. The simulation results agree very well with the empirical correlation for a spherical drop for all Re considered. The test results also affirm that the Stefan flow is important to the heat transfer between the drop and the surrounding vapor and also the vaporization rate. The drop volume loss due to vaporization will be overestimated if the Stefan flow is ignored.

Finally, a fully 3D simulation was performed for the aerodynamic breakup of an acetone drop in a high-speed and high-temperature vapor stream. The free-stream properties are similar to the post-shock conditions for a planar shock with Mach number 1.6, though the compressibility effect is not considered. With the help of adaptive mesh refinement, we were able to accurately resolve the drop surface and the temperature field near the interface. The minimum cell size in the octree mesh is equivalent to 256 cells across the initial drop diameter. Due to the high Weber number (We = 62.7), the drop breakup is in the multi-mode regime where the drop deforms to a Sombrero-hat shape, consisting of a backward bag at the center and a forward ring bag near the periphery. Eventually, the forward ring bag breaks, forming numerous small children droplets.

The vaporization rate of the drop initially agrees with the empirical correlation, which is expected, since the drop is still approximately spherical. As the drop deformation becomes significant, the increase of frontal surface area results in a significantly increased rate of vaporization. The decrease of drop volume in time becomes nonlinear and is much faster than the empirical correlation for a spherical drop. The present results indicated that the effects of We and drop deformation are important to drop vaporization if the drop Weber number

is finite, though a systematic parametric numerical investigation using the present simulation framework to fully characterize the effects of important parameters like We and Re will be relegated to our future work.

CRediT authorship contribution statement

Bradley Boyd: Formal analysis, Methodology, Software, Validation, Visualization, Writing – original draft. **Yue Ling:** Methodology, Writing – review & editing, Supervision, Funding acquisition.

Declaration of competing interest

The authors declare that they have no known competing financial interests or personal relationships that could have appeared to influence the work reported in this paper.

Data availability

Data will be made available on request.

Acknowledgments

This research was supported by the ACS Petroleum Research Fund (#62481-ND9). BB has been supported by the Baylor University Postdoctoral Hiring Program, while YL has also been partially supported by the NSF grant (#1942324). The authors also acknowledge the Extreme Science and Engineering Discovery Environment (XSEDE) and the Texas Advanced Computing Center (TACC) programs for providing the computational resources that have contributed to the research results reported in this paper. The Baylor High Performance and Research Computing Services (HPRCS) have been used to process the simulation data. The newly-developed methods have been implemented in the open-source multiphase flow solver *Basilisk*, which is made available by Stéphane Popinet and other collaborators.

References

- [1] Lefebvre AH, McDonell VG. Atomization and sprays. CRC Press; 2017.
- [2] Boyd B, Becker S. Numerical modeling of the acoustically driven growth and collapse of a cavitation bubble near a wall. *Phys Fluids* 2019;31(3):032102.
- [3] Boyd B, Becker S. Numerical modelling of an acoustically-driven bubble collapse near a solid boundary. *Fluid Dyn Res* 2018;50(6):065506.
- [4] Boyd B, Suslov SA, Becker S, Green tree AD, Maksymov IS. Beamed UV sonoluminescence by aspherical air bubble collapse near liquid-metal microparticles. *Sci Rep* 2020;10(1):1501.
- [5] Tryggvason G, Scardovelli R, Zaleski S. Direct numerical simulations of gas-liquid multiphase flows. Cambridge University Press; 2011.
- [6] Saurel R, Abgrall R. A multiphase Godunov method for compressible multifluid and multiphase flows. *J Comput Phys* 1999;150(2):425–67.
- [7] Johnsen E, Colonius T. Implementation of WENO schemes in compressible multicomponent flow problems. *J Comput Phys* 2006;219(2):715–32.

- [8] Boyd B, Jarrahdash D. A diffuse-interface method for reducing spurious pressure oscillations in multicomponent transcritical flow simulations. *Comput & Fluids* 2021;104924.
- [9] Boyd B, Jarrahdash D. Numerical study of the transcritical shock-droplet interaction. *Phys Rev Fluids* 2021;6(11):113601.
- [10] Scardovelli R, Zaleski S. Direct numerical simulation of free-surface and interfacial flow. *Annu Rev Fluid Mech* 1999;31(1):567–603.
- [11] Unverdi SO, Tryggvason G. A front-tracking method for viscous, incompressible, multi-fluid flows. *J Comput Phys* 1992;100:25–37.
- [12] Sussman M, Smereka P, Osher S. A level set approach for computing solutions to incompressible two-phase flow. *J Comput Phys* 1994;114:146–59.
- [13] Sher E, Bar-Kohany T, Rashkov A. Flash-boiling atomization. *Prog Energy Combust Sci* 2008;34:417–39.
- [14] Villegas LR, Tanguy S, Castanet G, Caballina O, Lemoine F. Direct numerical simulation of the impact of a droplet onto a hot surface above the Leidenfrost temperature. *Int J Heat Mass Transfer* 2017;104:1090–109.
- [15] Son JH, Park IS. Temperature changes around interface cells in a one-dimensional Stefan condensation problem using four well-known phase-change models. *Int J Therm Sci* 2021;161:106718.
- [16] Samkhaniani N, Ansari M. Numerical simulation of bubble condensation using CF-VOF. *Prog Nucl Energy* 2016;89:120–31.
- [17] Sazhin SS. Advanced models of fuel droplet heating and evaporation. *Prog Energy Combust Sci* 2006;32(2):162–214.
- [18] Shao C, Luo K, Chai M, Wang H, Fan J. A computational framework for interface-resolved DNS of simultaneous atomization, evaporation and combustion. *J Comput Phys* 2018;371:751–78.
- [19] Irfan M, Muradoglu M. A front tracking method for direct numerical simulation of evaporation process in a multiphase system. *J Comput Phys* 2017;337:132–53.
- [20] Safari H, Rahimian MH, Krafczyk M. Extended lattice Boltzmann method for numerical simulation of thermal phase change in two-phase fluid flow. *Phys Rev E* 2013;88(1):013304.
- [21] Haghani-Hassan-Abadi R, Fakhri A, Rahimian M-H. Phase-change modeling based on a novel conservative phase-field method. *J Comput Phys* 2021;432:110111.
- [22] Gibou F, Chen L, Nguyen D, Banerjee S. A level set based sharp interface method for the multiphase incompressible Navier–Stokes equations with phase change. *J Comput Phys* 2007;222(2):536–55.
- [23] Lee MS, Riaz A, Aute V. Direct numerical simulation of incompressible multiphase flow with phase change. *J Comput Phys* 2017;344:381–418.
- [24] Welch SW, Wilson J. A volume of fluid based method for fluid flows with phase change. *J Comput Phys* 2000;160(2):662–82.
- [25] Hardt S, Wondra F. Evaporation model for interfacial flows based on a continuum-field representation of the source terms. *J Comput Phys* 2008;227(11):5871–95.
- [26] Ma C, Bothe D. Numerical modeling of thermocapillary two-phase flows with evaporation using a two-scalar approach for heat transfer. *J Comput Phys* 2013;233:552–73.
- [27] Sato Y, Nićeno B. A sharp-interface phase change model for a mass-conservative interface tracking method. *J Comput Phys* 2013;249:127–61.
- [28] Perez-Raya I, Kandlikar SG. Modeling of evaporation phenomenon considering liquid and vapor phase conduction effects: Stefan problems. In: ASME 2016 14th international conference on nanochannels, microchannels, and minichannels. Vol. 1, Washington, DC, USA: American Society of Mechanical Engineers; 2016, p. 1.
- [29] Datta P, Chakravarty A, Ghosh K, Mukhopadhyay A, Sen S. Modeling aspects of vapor bubble condensation in subcooled liquid using the VOF approach. *Numer Heat Transf A: Appl* 2017;72(3):236–54.
- [30] Ding S-T, Luo B, Li G. A volume of fluid based method for vapor-liquid phase change simulation with numerical oscillation suppression. *Int J Heat Mass Transfer* 2017;110:348–59.
- [31] Wilson JA, Haghshenas M, Kumar R. Phase-change mechanism for evaporation in porous media using volume of fluid: Implicit formulation of interfacial temperature. *Int Commun Heat Mass Transfer* 2019;103:90–9.
- [32] Wang Y, Yang V. Vaporization of liquid droplet with large deformation and high mass transfer rate, I: Constant-density, constant-property case. *J Comput Phys* 2019;392:56–70.
- [33] Palmore J, Desjardins O. A volume of fluid framework for interface-resolved simulations of vaporizing liquid-gas flows. *J Comput Phys* 2019;399:108954.
- [34] Scapin N, Costa P, Brandt L. A volume-of-fluid method for interface-resolved simulations of phase-changing two-fluid flows. *J Comput Phys* 2020;407:109251.
- [35] Bureš L, Sato Y. Direct numerical simulation of evaporation and condensation with the geometric VOF method and a sharp-interface phase-change model. *Int J Heat Mass Transfer* 2021;173:121233.
- [36] Malan L, Malan A, Zaleski S, Rousseau P. A geometric VOF method for interface resolved phase change and conservative thermal energy advection. *J Comput Phys* 2021;426:109920.
- [37] Kharangate CR, Mudawar I. Review of computational studies on boiling and condensation. *Int J Heat Mass Transfer* 2017;108:1164–96.
- [38] Tryggvason G, Esmaeeli A, Al-Rawahi N. Direct numerical simulations of flows with phase change. *Comput Struct* 2005;83(6–7):445–53.
- [39] Gao X, Chen J, Qiu Y, Ding Y, Xie J. Effect of phase change on jet atomization: a direct numerical simulation study. *J Fluid Mech* 2022;935:A16.
- [40] Zhao S, Zhang J, Ni M-J. Boiling and evaporation model for liquid-gas flows: A sharp and conservative method based on the geometrical VOF approach. *J Comput Phys* 2022;452:110908.
- [41] Johansen H, Colella P. A cartesian grid embedded boundary method for poisson's equation on irregular domains. *J Comput Phys* 1998;147(1):60–85.
- [42] Schwartz P, Barad M, Colella P, Ligocki T. A Cartesian grid embedded boundary method for the heat equation and Poisson's equation in three dimensions. *J Comput Phys* 2006;211(2):531–50.
- [43] Hsiang L-P, Faeth GM. Drop deformation and breakup due to shock wave and steady disturbances. *Int J Multiph Flow* 1995;21:545–60.
- [44] Theofanous TG, Li GJ. On the physics of aerobreakup. *Phys Fluids* 2008;20(5):052103.
- [45] Meng JC, Colonius T. Numerical simulation of the aerobreakup of a water droplet. *J Fluid Mech* 2018;835:1108.
- [46] Jain SS, Tyagi N, Prakash RS, Ravikrishna R, Tomar G. Secondary breakup of drops at moderate Weber numbers: Effect of Density ratio and Reynolds number. *Int J Multiph Flow* 2019;117:25–41.
- [47] Jackiw IM, Ashgriz N. On aerodynamic droplet breakup. *J Fluid Mech* 2021;913:A33.
- [48] Duke-Walker V, Maxon WC, Almuhna SR, McFarland JA. Evaporation and breakup effects in the shock-driven multiphase instability. *J Fluid Mech* 2021;908:A13.
- [49] Dahal J, McFarland JA. A numerical method for shock driven multiphase flow with evaporating particles. *J Comput Phys* 2017;344:210–33.
- [50] Gallot-Lavallée S, Jones WP, Marquis AJ. Large eddy simulation of an ethanol spray flame with secondary droplet breakup. *Flow Turbul Combust* 2021;107(3):709–43.
- [51] Salman H, Soteriou M. Lagrangian simulation of evaporating droplet sprays. *Phys Fluids* 2004;16(12):4601–22.
- [52] Maxey MR, Riley JJ. Equation of motion for a small rigid sphere in a nonuniform flow. *Phys Fluids* 1983;26:883–9.
- [53] Balachandar S, Eaton JK. Turbulent dispersed multiphase flow. *Annu Rev Fluid Mech* 2010;42:111–33.
- [54] Renksizbulut M, Yuen MC. Experimental study of droplet evaporation in a high-temperature air stream. *J Heat Transfer* 1983;105(2):384–8.
- [55] Popinet S, Gerris: a tree-based adaptive solver for the incompressible Euler equations in complex geometries. *J Comput Phys* 2003;190(2):572–600.
- [56] Popinet S. An accurate adaptive solver for surface-tension-driven interfacial flows. *J Comput Phys* 2009;228(16):5838–66.
- [57] Popinet S. A quadtree-adaptive multigrid solver for the Serre–Green–Naghdi equations. *J Comput Phys* 2015;302:336–58.
- [58] Zhang B, Popinet S, Ling Y. Modeling and detailed numerical simulation of the primary breakup of a gasoline surrogate jet under non-evaporative operating conditions. *Int J Multiph Flow* 2020;130:103362.
- [59] Zhang B, Boyd B, Ling Y. Direct numerical simulation of compressible interfacial multiphase flows using a mass-momentum-energy consistent volume-of-fluid method. *Comput & Fluids* 2021;105267.
- [60] Georgoulas A, Andredaki M, Marengo M. An enhanced VOF method coupled with heat transfer and phase change to characterise bubble detachment in saturated pool boiling. *Energies* 2017;10(3):272.
- [61] Weymouth G, Yue DK-P. Conservative Volume-of-Fluid method for free-surface simulations on Cartesian-grids. *J Comput Phys* 2010;229(8):2853–65.
- [62] Fuster D, Popinet S. An all-Mach method for the simulation of bubble dynamics problems in the presence of surface tension. *J Comput Phys* 2018;374:752–68.
- [63] Francois MM, Cummins SJ, Dendy ED, Kothe DB, Sicilian JM, Williams MW. A balanced-force algorithm for continuous and sharp interfacial surface tension models within a volume tracking framework. *J Comput Phys* 2006;213:141–73.
- [64] van Hoof JA, Popinet S, van Heerwaarden CC, van der Linden SJA, de Roode SR, van de Wiel BJH. Towards adaptive grids for atmospheric boundary-layer simulations. *Bound-Lay Meteorol* 2018;167(3):421–43.
- [65] Aulisa E, Manservisi S, Scardovelli R, Zaleski S. Interface reconstruction with least-squares fit and split advection in three-dimensional Cartesian geometry. *J Comput Phys* 2007;225(2):2301–19.
- [66] Vaudor G, Ménard T, Aniszezwski W, Doring M, Berlemont A. A consistent mass and momentum flux computation method for two phase flows. Application to atomization process. *Comput & Fluids* 2017;152:204–16.
- [67] Arrufat T, Criales-Esposito M, Fuster D, Ling Y, Malan L, Pal S, et al. A momentum-conserving, consistent, Volume-of-Fluid method for incompressible flow on staggered grids. *Comput & Fluids* 2020;215:104785.
- [68] López-Herrera J, Gafán-Calvo A, Popinet S, Herrada M. Electrokinetic effects in the breakup of electrified jets: A Volume-Of-Fluid numerical study. *Int J Multiph Flow* 2015;71:14–22.
- [69] Bell JB, Colella P, Glaz HM. A second-order projection method for the incompressible navier-stokes equations. *J Comput Phys* 1989;85(2):257–83.
- [70] Lalanne C, Magdelaine Q, Lequien F, Fullana J-M. Numerical model using a Volume-of-Fluid method for the study of evaporating sessile droplets in both unpinned and pinned modes. *Eur J Mech B/Fluids* 2021;89:267–73.

- [71] Berenson PJ. Film-boiling heat transfer from a horizontal surface. *J Heat Transfer* 1961;83(3):351–6.
- [72] Klimenko V. Film boiling on a horizontal plate — new correlation. *Int J Heat Mass Transfer* 1981;24(1):69–79.
- [73] Sun D, Xu J, Chen Q. Modeling of the evaporation and condensation phase-change problems with FLUENT. *Numer Heat Transfer B* 2014;66(4):326–42.
- [74] Esmaeeli A, Tryggvason G. Computations of film boiling. Part I: numerical method. *Int J Heat Mass Transfer* 2004;47(25):5451–61.
- [75] Tomar G, Biswas G, Sharma A, Agrawal A. Numerical simulation of bubble growth in film boiling using a coupled level-set and volume-of-fluid method. *Phys Fluids* 2005;17(11):112103.
- [76] Guo DZ, Sun DL, Li ZY, Tao WQ. Phase Change Heat Transfer Simulation for Boiling Bubbles Arising from a Vapor Film by the VOSET Method. *Numer Heat Transf A: Appl* 2011;59(11):857–81.
- [77] Pilch M, Erdman CA. Use of breakup time data and velocity history data to predict the maximum size of stable fragments for acceleration-induced breakup of a liquid drop. *Int J Multiph Flow* 1987;13:741–57.
- [78] Hsiang L-P, Faeth GM. Near-limit drop deformation and secondary breakup. *Int J Multiph Flow* 1992;18:635–52.
- [79] Joseph DD, Belanger J, Beavers GS. Breakup of a liquid drop suddenly exposed to a high-speed airstream. *Int J Multiph Flow* 1999;25(6):1263–303.
- [80] Guildenbecher DR, López-Rivera C, Sojka PE. Secondary atomization. *Exp Fluids* 2009;46(3):371.
- [81] Theofanous TG, Mitkin VV, Ng CL, Chang CH, Deng X, Sushchikh S. The physics of aerobreakup. II. Viscous liquids. *Phys Fluids* 2012;24:022104.
- [82] Mahmood TH, Ling Y. Effects of Reynolds number on aerobreakup of viscous drops. In: Proceedings of ICLASS 2021: 15th triennial international conference on liquid atomization and spray systems. Vol. 1, 2021, p. 1.
- [83] Balachandar S. A scaling analysis for point particle approaches to turbulent multiphase flows. *Int J Multiph Flow* 2009;35:801–10.
- [84] Wert KL. A rationally-based correlation of mean fragment size for drop secondary breakup. *Int J Multiph Flow* 1995;21:1063–71.
- [85] Dai Z, Faeth GM. Temporal properties of secondary drop breakup in the multimode breakup regime. *Int J Multiph Flow* 2001;27:217–36.
- [86] Kuo C-W, Trujillo MF. A maximum entropy formalism model for the breakup of a droplet. *Phys Fluids* 2022;34(1):013315.
- [87] Ranger AA, Nicholls JA. Aerodynamic shattering of liquid drops. *AIAA J* 1969;7:285–90.
- [88] Haywood RJ, Nafziger R, Renksizbulut M. A detailed examination of gas and liquid phase transient processes in convective droplet evaporation. *J Heat Transfer* 1989;111(2):495–502.
- [89] Chiang CH, Raju MS, Sirignano WA. Numerical analysis of convecting, vaporizing fuel droplet with variable properties. *Int J Heat Mass Transfer* 1992;18.
- [90] Yuen M, Chen L. Heat-transfer measurements of evaporating liquid droplets. *Int J Heat Mass Transfer* 1978;21(5):537–42.
- [91] Renksizbulut M, Yuen MC. Numerical study of droplet evaporation in a high-temperature stream. *J Heat Transfer* 1983;105(2):389–97.
- [92] Marcotte F, Zaleski S. Density contrast matters for drop fragmentation thresholds at low Ohnesorge number. *Phys Rev Fluids* 2019;4(10):103604.
- [93] Herrmann M. A parallel Eulerian interface tracking/Lagrangian point particle multi-scale coupling procedure. *J Comput Phys* 2010;229:745–59.
- [94] Ling Y, Zaleski S, Scardovelli R. Multiscale simulation of atomization with small droplets represented by a Lagrangian point-particle model. *Int J Multiph Flow* 2015;76:122–43.
- [95] Zuzio D, Estivalezes J-L, DiPierro B. An improved multiscale Eulerian-Lagrangian method for simulation of atomization process. *Comput & Fluids* 2018;176:285–301.